Temperature and Salt Advection in Oceanic Models

M. Iskandarani and E. Chassignet

Rosenstiel School of Marine and Atmospheric Science, U. of Miami, Miami FL 33149

September 24, 2002

Abstract

We investigate the impact of numerical approximations on the evolution of temperature and salt, and by implication, density, in ocean models. Several finite-difference based schemes are tested in problems with varying degree of difficulties.

1 Introduction

Modeling the evolution of temperature and salt distribution in the ocean is one of the main computational issues in oceanic simulations. The problem lies in the inherent difficulties associated with integrating an advection-diffusion equation in the inviscid and advection dominated regimes. The problems are well-known and are reflected by the properties that an ideal advection scheme would possess besides stabillity and consistency: conservation, shape preservation, phase accuracy, minimal numerical dissipation, monotonicity, and last but not least computational efficiency.

In addition to the properties mentioned above, an additional constraint comes up when considering the transport of coupled species. In the oceanic case, temperature, and salt concentration determine density via the equation of state. For a particle moving along an isopycnal surface, its temperature and salt content must change so as to keep its density constant. This constraint is very difficult, if not impossible, to impose on numerical models that evolve the temperature and salt tracers independently, and where the density is diagnosed from the tracers distribution. Numerical errors in the tracer advection step lead to density anomalies where none is expected physically. We will refer to these anomalies as numerical cabbeling in analogy to the physical cabbeling that occurs when water parcels of differing T/S properties, but equal densities, combine to yield denser water owing to the nonlinearity of the equation of state. The latter is essential for numerical cabbeling as discussed below.

This article is primarily concerned with the impact of the tracer advection schemes on numerical cabbeling. Section 2 discusses briefly the equations governing the evolution of the T/S fields and the conditions which will inhibit cabbeling. Section 3 illustrates numerical cabbeling in simple one-dimensional flows, and highlights the different aspects of a numerical scheme that can impact it, namely high versus low order spatial differencing, and the role of TVD limiters. The majority of the article is devoted to quantifying numerical cabbeling in a two dimensional idealized double gyre circulation in a square basin; the details of the flow are presented in section 4. Four different representative advection schemes are tested on typical salt and temperature distributions chosen along an initially isopycnic layer. The temperature and salt are then advected independently and the ensuing density is diagoned. The advection schemes are listed in section 5, and the numerical results are presented in sections 6, 7, and 8.

2 Background

Before we begin our discussion of numerical cabbeling we first set the stage by reviewing the equations governing the evolution of density in the ocean. The derivation of these equations from general physical and thermodynamic principles is actually quite complicated. The difficulties stem from the nonhomogeneous nature of the fluid caused by the presence of salt. Most introductory textbooks gloss over these complications and consider the case of a homogeneous incompressible fluid where the state variables are density, temperature and pressure only. The two primary principles invoked are the conservation of mass and internal energy (see appendix A). Since water in the ocean is incompressible, mass conservation reduces to volume conservation. Various thermodynamic relationships can then invoked to transform the internal energy equation into a temperature evolution equation. Finally the principle of salt conservation is invoked to derived an evolution equation for the salt concentration. Density in oceanic models depends thus on the temperature and salt conservation equations, and the equation of state. Implicit in this derivation is the assumption that the inclusion of salt in the equation of state does not add substantial terms to the temperature conservation equation.

The temporal evolution of density in traditional oceanic models (hydrostatic, incompressible, and Boussinesq approximation) is governed by the equation of state:

$$\rho = \rho(T, S, p), \tag{1}$$

where ρ is the density, p is the pressure, T the (potential) temperature, and S the salt concentration; and the conservation equations for temperature and salt:

$$\frac{\mathrm{d}T}{\mathrm{d}t} = \kappa_T \nabla^2 T + Q_T \tag{2}$$

$$\frac{\mathrm{d}S}{\mathrm{d}t} = \kappa_S \nabla^2 S + Q_S \tag{3}$$

where κ_T and κ_S represent diffusion coefficients for temperature and salt, respectively. Note that in large scale ocean models these coefficients represent eddy diffusion coefficients and are usually taken to be equal, even though their molecular counter parts differ by 2 orders of magnitudes. The particular details of the dissipation operator (the Laplacian operator here) is not important for the present discussion as long it is linear. Q_T and Q_S represent sources of heat and salt.

A density evolution equation can be derived by taking the total derivative of the equation of state:

$$\begin{aligned}
\frac{\mathrm{d}\rho}{\mathrm{d}t} &= \frac{\partial \rho}{\partial T}\frac{\mathrm{d}T}{\mathrm{d}t} + \frac{\partial \rho}{\partial S}\frac{\mathrm{d}S}{\mathrm{d}t} + \frac{\partial \rho}{\partial p}\frac{\mathrm{d}p}{\mathrm{d}t} && (4) \\
&= -\alpha\frac{\mathrm{d}T}{\mathrm{d}t} + \beta\frac{\mathrm{d}S}{\mathrm{d}t} && (5) \\
&= -\alpha\kappa_T\nabla^2 T + \beta\kappa_S\nabla^2 S - \alpha Q_T + \beta Q_S && (6)
\end{aligned}$$

where α and β are the thermal expansion and haline contraction coefficients, respectively; the third term on the right hand side of equation 4 has been dropped on account of the incompressibility assumption. The coefficients α and β are constant for a linear equation of state. Equation (6) shows that in the absence of heat and salt sources ($Q_T = Q_S = 0$) tracer mixing leads to density variations. If no mixing takes place, $\kappa_T = \kappa_S = 0$, a fluid particle retains its density as it moves about in the fluid. This conclusion holds independently of the particular form of the equation of state, linear or nonlinear.

The present article is primarily concerned with density variations due to cabbeling, i.e. density changes due to the mixing of water masses of approximately equal densities but different T/S properties. Equation 6 can be used to establish the necessary conditions for cabbeling to be *absent*, namely a linear equation of state, and $\kappa_T = \kappa_S = \kappa$. To see this, we assume a linear equation of state of the form:

$$\rho = \rho_0 - \alpha T + \beta S, \tag{7}$$

and we rewrite equation 6 as

$$\frac{\mathrm{d}\rho}{\mathrm{d}t} = \kappa \nabla^2 \left(\rho_0 - \alpha T + \beta S\right). \tag{8}$$

If the initial distribution of T/S is such that a constant density is produced, the right hand side of equation (8) is zero, and a particle will retain its density. A nonlinear equation of state is essential for cabbeling even in the presence of mixing.

Our primary concern in the present paper is to quantify the amount of numerical cabbeling that can occur in an ocean model. This cabbeling is triggered by the numerical dissipation inherent in numerical schemes used to integrate the tracer equations. In particular, strongly stable method that rely on flux and slope limiters to prevent Gibbs oscillations near front, can kick up the numerical dissipation susbtantially in regions of strong tracer gradients.

3 One Dimensional Experiments

We illustrate numerical cabbeling by considering the simple problem of the advection of two tracers (temperature and salinity) in a one dimensional periodic channel of unit width by a constant velocity field:

$$\frac{\partial T}{\partial t} + \frac{\partial T}{\partial x} = 0 \tag{9}$$

$$\frac{\partial S}{\partial t} + \frac{\partial S}{\partial x} = 0 \tag{10}$$

The initial condition on the salinity field is chosen to be a Gaussian hill with decay length scale of 1/16.

$$S(x, t = 0) = 1.5e^{-256x^2} + 34.5. \tag{11}$$

The initial temperature field is determined by requiring that the T/S combination yields a constant density field of $\rho_0 = 27.5$ sigma units. The T/S fields are independently advected for one period; and the density implied by the tracers at the final time step is calculated.

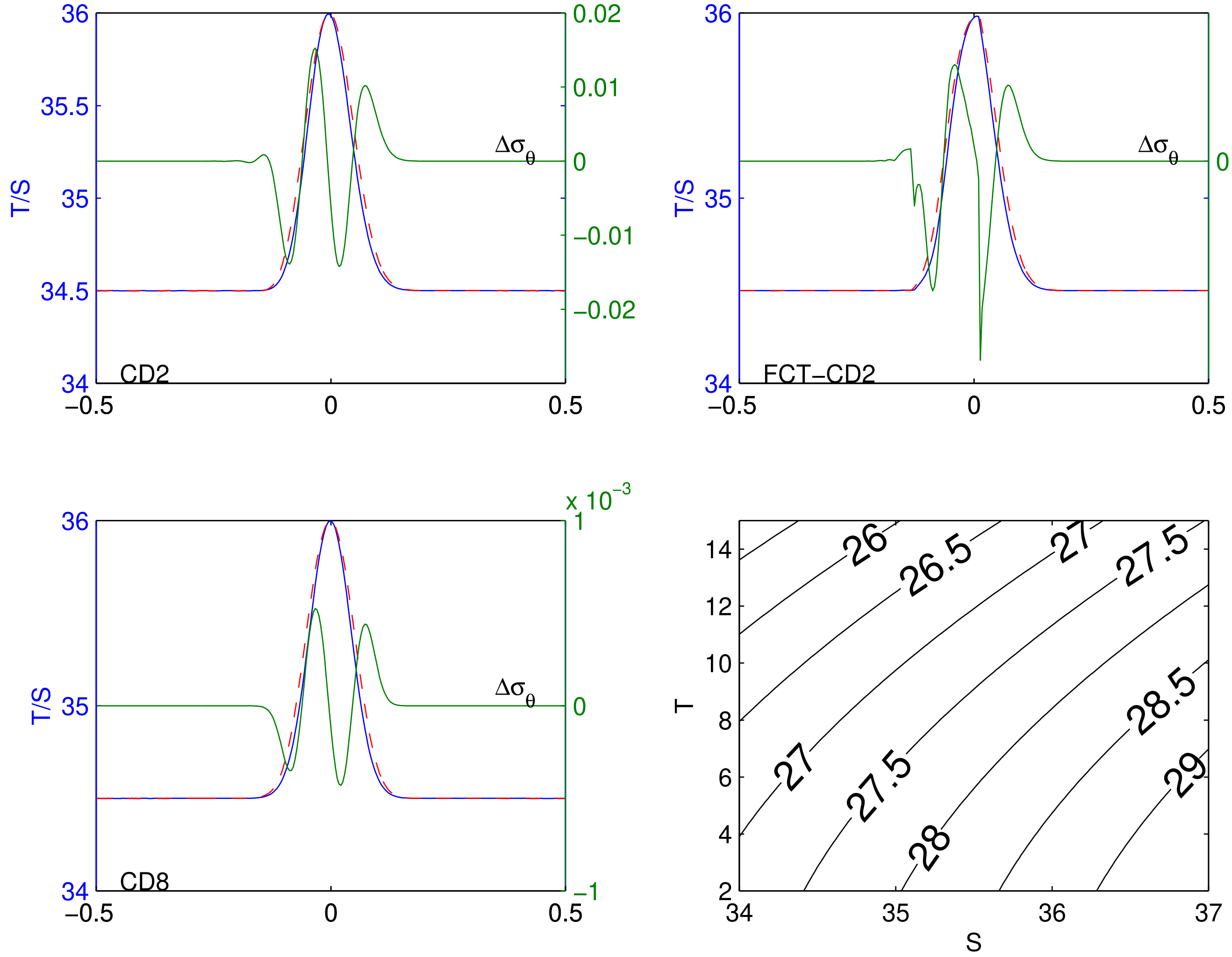

Figure 1: Plot of T/S fields (left axis) at the end of the simulation and the implied density error $\Delta\sigma_\theta$ (right axis) at the end of one rotation. The temperature field is in red dashed lines and has been scaled so as to have the same range as the salinity field for plotting purposes. The density anomaly is shown in green in sigma units (right axis). The numerical schemes used centered differences in space: 2nd order (upper left), 8th order (lower left), and FCT 2nd order (upper right); the time stepping was leap-frog trapezoidal. The density scales are identical for CD2 and FCTCD2 (the top 2 panels). The TS diagram is also shown for reference in the lower right panel.

The density anomalies are shown in figure 1 for several traditional centered-space advection schemes, namely, a second order scheme (CD2), a second order scheme with a flux corrected transport algorithm (FCT-CD2), and an eigth order scheme (CD8). The time differencing is leapfrog-trapezoidal. The CD2 scheme has been the workhorse of most ocean models owing to its good phase and dissipation properties (a pure leap-frog scheme would display no numerical dissipation) but would require occasional filtering to damp the computational mode (a form of dissipation). The CD2 scheme produces Gibbs oscillations in the vicinity of under-resolved fronts; these oscillations can be eliminated with the help of FCT; the CD2-FCT scheme is representative of the total variation diminishing (TVD) class of schemes. Note that in spite of the smoothness of the initial data, a vanilla FCT implementation will activate its limiter near the tracer peaks. Finally, the eighth order scheme is included to investigate the impact of high order spatial differencing on numerical cabbeling.

The numerical parameters are $\Delta t = 10^{-3}$, $\Delta x = 1/256$, and the Courant number is 0.256. The equation of state is nonlinear and is the one used in HYCOM. The degree of nonlinearity in the equation of state is reflected in the curvature of the 27.5 contour lines in the TS diagram shown in the right panel of figure 1.

It is clear the density anomaly can be significant even in this exceedingly simple case. The magnitude of the maximum density anomaly in the second order scheme is 0.015 sigma units. The error can be decreased by using higher order spatial differencing: an eighth order scheme reduces the maximum error by a factor of 50. Limiters tend to increase the magnitude of the density anomaly as illustrated in the FCT experiment. The extrema clipping characteristics of most flux limiters has essentially doubled the density anomaly near the tracer peaks. The density anomaly is due to the numerical discretization error *and* the nonlinearity of the equaiton of state. A similar test using a linear equation of state produced no density anomaly (to machine precision). In the following section we derive the conditions that a one-dimensional numerical scheme should fullfill in order to prevent numerical cabbeling.

A typical discretization of the tracer advection equations in one spatial dimension can be written as follows:

$$T_i^{n+1} = T_i^n + \sum_{j=-l}^{r} c_j^T T_{i+j}^n \tag{12}$$

$$S_i^{n+1} = S_i^n + \sum_{j=-l}^{r} c_j^S S_{i+j}^n \tag{13}$$

where the c_j^T and c_j^S are coefficients that depends on the advecting velocity and the particular finite difference scheme. We assume that the same advection scheme is used for T/S. The stencil used to update the tracers uses l grid points to the left of node i and r grid points to the right of point i. In the case where the scheme is linear (no limiters) the coefficients are independent of T and S, and hence $c_j^T = c_j^S$. Given an equation of state of the form

$$\rho(T,S) = \rho_0 - \alpha T + \beta S + \gamma T^2, \tag{14}$$

where γ is our token, but illustrative, nonlinearity, the density at the new time level is:

$$\rho_i^{n+1} = \rho_i^n + \sum_{j=-l}^{r} \left(-c_j^T \alpha T_{i+j}^n + c_j^S \beta S_{i+j}^n \right)$$

$$+ \quad \gamma \left[2T_i^n \left(\sum_{j=-l}^{r} c_j^T \alpha T_{i+j}^n \right) + \sum_{j=-l}^{r} \sum_{k=-l}^{r} c_j^T c_k^T T_{i+j}^n T_{i+k}^n \right] \qquad (15)$$

If the density field is originally constant it should remain constant under advection. The equation above permits to list sufficient conditions under which this constraint is satisfied:

- The equation of state must be linear, i.e. $\gamma = 0$.
- The finite difference scheme is linear and $c_j^T = c_j^S = c_j$. Then, and for a linear equation of state, the density at the new time level can be rewritten in the form:

$$\rho_i^{n+1} = \rho_i^n + (\rho_i^n - \rho_0) \sum_{j=-l}^{r} c_j \qquad (16)$$

  where the constant density anomaly was factored out of the summation sign.
- The final condition is then that the numerical scheme be constancy preserving, i.e. $\sum_{j=-l}^{r} c_j = 0$.

Note that the task of eliminating density sources for a nonlinear equation of state requires modifying the advection scheme's coefficients, $c_j^T = c_j^S$, without affecting the scheme's other basic properties such as consistency, stability and conservation.

4 Two Dimensional Experiments

Our two dimensional cabbeling experiments revolve around the flow associated with a wind-driven, double gyre circulation in a square basin. This configuration was chosen because it is more representative of oceanic flows then the ones found in standard advection tests such as the rotating cone and deformational flow [11] experiments. It includes in particular a western boundary current and a recirculation zone where initially smooth tracers distribution are rapidly strained and deformed.

An added consideration concerns the solenoidal nature of the flow field and its associated mass conservation equation [13]. In cases where the flow is solenoidal and the computational grid is fixed in time, the flux form and advective form of the tracer equations are equivalent. The mass conservation equation is substantially more complicated in modern ocean models owing to the motion of the computational grid where it takes the form

$$h_t + \nabla \cdot (h\mathbf{u}) = 0 \qquad (17)$$

Here h can represent the layer thickness or pressure difference, and $\mathbf{u}$ the advecting velocity. Under these conditions the flux form of the advection equations is

$$(Th)_t + \nabla \cdot (Th\mathbf{u}) = 0 \qquad (18)$$

The analytical prescription of a non-trivial non-solenoidal flow field is complicated by the form of the equation. Here we revert to a standard numerical solution of the shallow water equation [8] to prescribe a steady non-solenoidal flow field. This solution represents the double gyre, wind-driven circulation in a square basin. The basin is 2000x2000 km^2 and has constant depth $h = 500$ m. It is located on a β-plane with

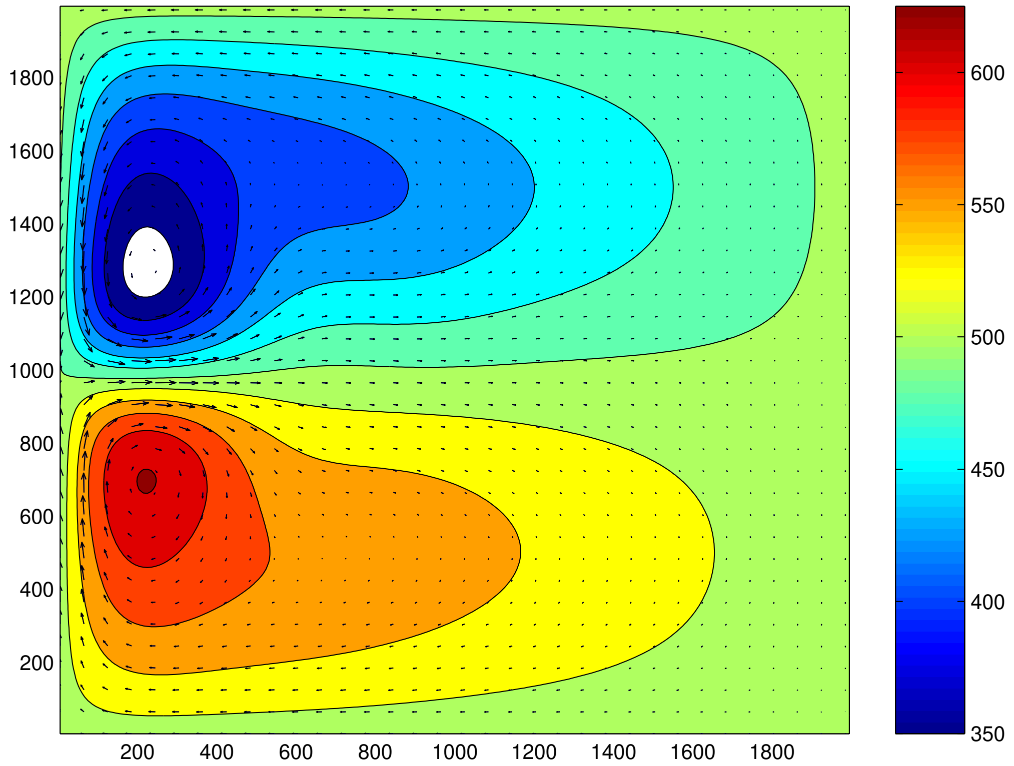

Figure 2: Layer thickness and vector plot of the velocity at steady state

the following parameter $f_0 = 9 \times 10^{-5}$ s^{-1} at mid-latitude and $\beta = 1.8 \times 10^{-11}$ 1/ms; reduced gravity was set to 0.05 m/s^2. The wind stress is zonal and given by

$$\tau^x = -\tau \cos\left(2\pi \frac{y}{L}\right) \tag{19}$$

where $\tau = 0.1$ dynes, and L is the meridional size of the basin. The dissipation was provided by a Laplacian viscosity of 10000 m^2/s. The relevant dynamical scales for the above values of the physical parameters are the Rossby radius $R = \sqrt{gh}/f = 50$ km, and the Munk layer thickness is 82 km. (The large value of viscosity was chosen to eliminate eddying motion and reach a steady state fast). The equations were integrated numerical until a steady state was reached. The numerical parameters were as follows $\Delta x = \Delta y = 10$ km, and $\Delta t = 20$ minutes. The layer thickness and vector velocities at steady state are shown in figure 2.

5 Advection Schemes

The advection schemes tested are: Smolarkiewicz's MPDATA in its second order form, a fourth order centered difference scheme with leapfrog-trapezoidal time stepping, UTOPIA, and WENO. In the following we present an overview of these schemes and give some details to their implementation in our numerical experiments.

5.1 Centered Schemes with FCT

This scheme relies on fourth order centered differences in space, and second order centered differences in time to approximate the partial derivatives appearing in the equations. It is well-known for its excellent phase and amplitude perservation properties ([3]). Its drawback is the need to filter out the computational mode generated by the leap-frog differencing. In our tests, we have used a Leap-Frog trapezoidal time-integration to control the computational mode at the cost of introducing a small numerical dissipation. This scheme is complemented with Flux Correction in order to eliminate Gibbs oscillations near under-resolved gradients; the FCT algorithm has been implemented as in Zalesak [14].

5.2 MPDATA of Smolarkiewicz

The Multidimensional Positive Definite Advection and Transport Algorithm (MPDATA; see [10] and references therein) has been the work-horse of MICOM for the integration of the tracer equations. The scheme is based on multiple predictor-corrector applications of the donor cell scheme. The scheme preserves positivity by design. Gibbs oscillations near steep gradients are avoided with flux correction a la FCT.

5.3 UTOPIA

The Uniform Third Order Polynomial Interpolation Algorithm (UTOPIA) is representative of the upstream biased Eulerian advection scheme [5, 7]. The scheme is based on a finite volume formulation. Its distinguishing feature is that the flux computation relies on a Lagrangian description of the fluid entering the control volume cells: the fluxes through the faces are estimated by integrating the transported variable over the volume swept up by the advective velocity field. The scheme relies on quadratic polynomial interpolation for its reconstruction procedure and is, formally, third order accurater when the flow field is uniform. The scheme performs better then second order scheme even when the flow is not uniform. In our experiments we use the Rasch [7] form of the scheme, and implement the Universal Limiter of Thuburn [13] to eliminate Gibbs oscillations.

5.4 WENO

Traditional high order non-oscillatory finite difference/finite volume scheme degenerate to first order accuracy near discontinuities. Weighed Essentially Non-Oscillatory (WENO) [9] schemes are designed to extend high order accuracy right up to the discontinuity by shifting their interpolation stencil according to the smoothness of the solution. Although WENO schemes do allow oscillations, the latter's amplitude decays as a high power of the grid spacing. Recent modifications to the basic WENO procedure allow the enforcement of monotonicity constraints [1, 12]. WENO schemes are most useful in long term integration where their good phase property and low numerical dissipation make them superior to low order method. We include them in our suite of experiments to illustrate the impact of high order methods on numerical cabbeling. A second order TVD Runge-Kutta method [4] was used for the time integration. Our particular WENO experiments relied on a finite volume formulation of the problem.

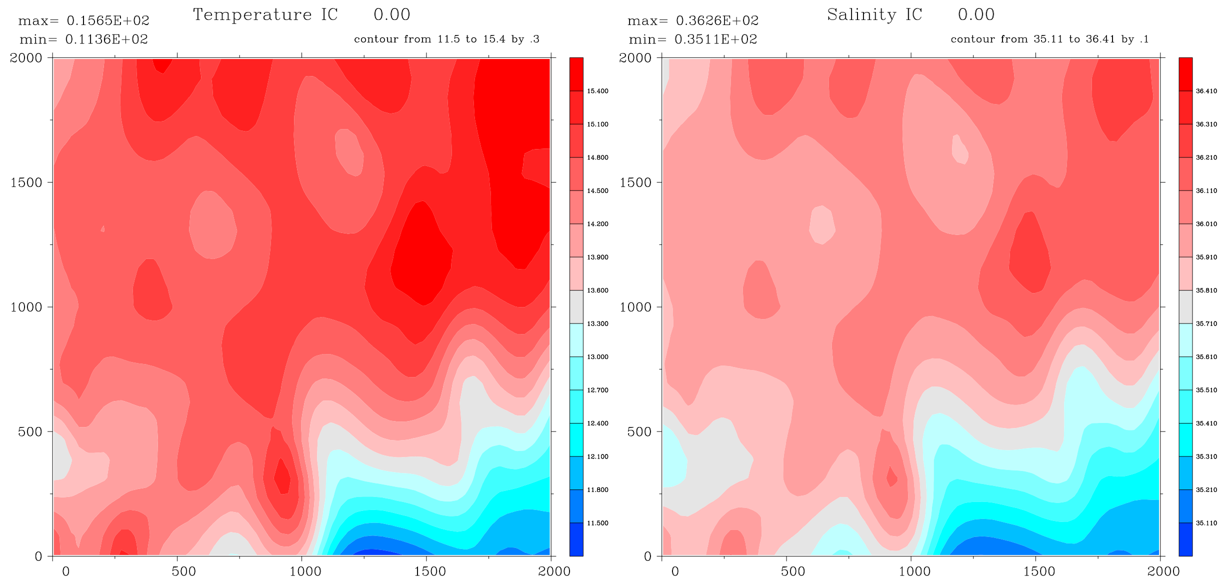

Figure 3: Initial conditions for the Levitus T/S fields whose combination yields a constant density of 26.8 sigma units.

We have avoided the computations of the cell boundary integrals in our implementation WENO to reduce the number of (expensive) reconstruction procedures. This approximation amounts to assuming that the flow field is spatially uniform in the cell's neighborhood. The major drawback of WENO schemes are their computational expense (on a per grid point basis) compared to low order method. The high cost is mainly due to the evaluation of the smoothness criteria. Our experiments rely on a very high nineth order scheme in space, and no limiters were used.

6 Levitus T/S

The initial conditions for the temperature and salinity fields were obtained from the one-degree Levitus data set. The sample region was taken to be in the tropical eastern Atlantic. (*Note: the choice of region was one of pure convenience: it was the largest tropical zone uninterrupted by masking. Must ask Linda for the lon-lat extent of the region)*. The T/S field combine to yield a density of 26.8. This layer is present in the subtropical gyre and has an average depth of 600 m. The initial conditions for the temperature and salinity are shown in figure 3. The salinity minimum is located in the south-east portion of the basin. There are several local maxima located primarily in the north east part of the basin. Both fields are smooth.

The salinity field at the end of a 180 day simulation is shown in figure 4 for the different schemes used. A reference solution using the method of characteristic is also shown in the bottom left panel. Note that the characteristic solution is not exact since I needed to interpolate the velocity field during the calculation of the trajectory, and the tracer fields when the foot of the characteristic was reached. In both instances I used a fourth order polynomial interpolation. The large scale features of the different solutions are similar. The most noticeable differences concern the location of the salinity extrema

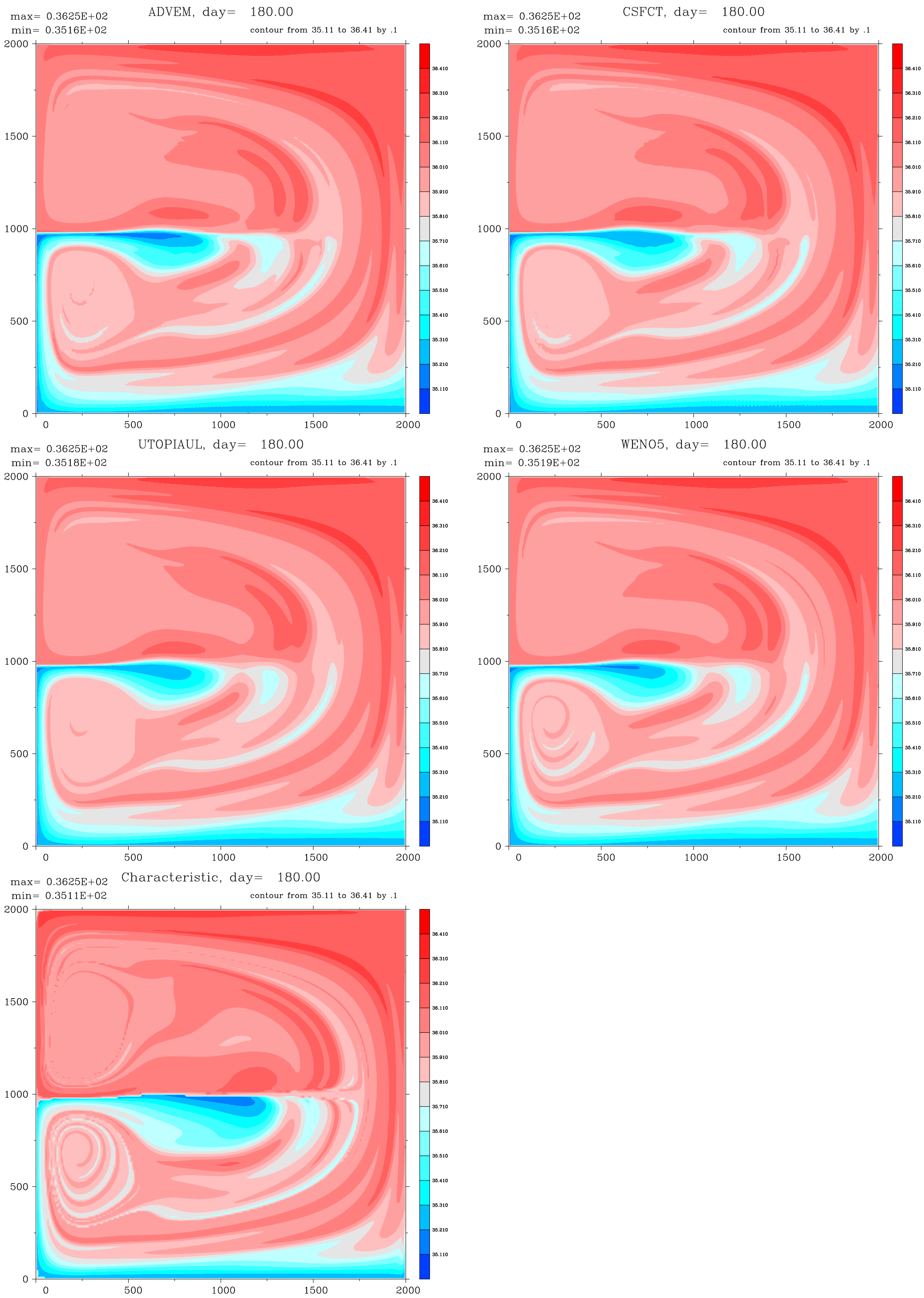

Figure 4: Salinity at the end of the simulation. In row order from top to bottom we have ADVEM, CSFCT, UTOPIA-UL, WENO5, and the characteristic solution shown for reference.

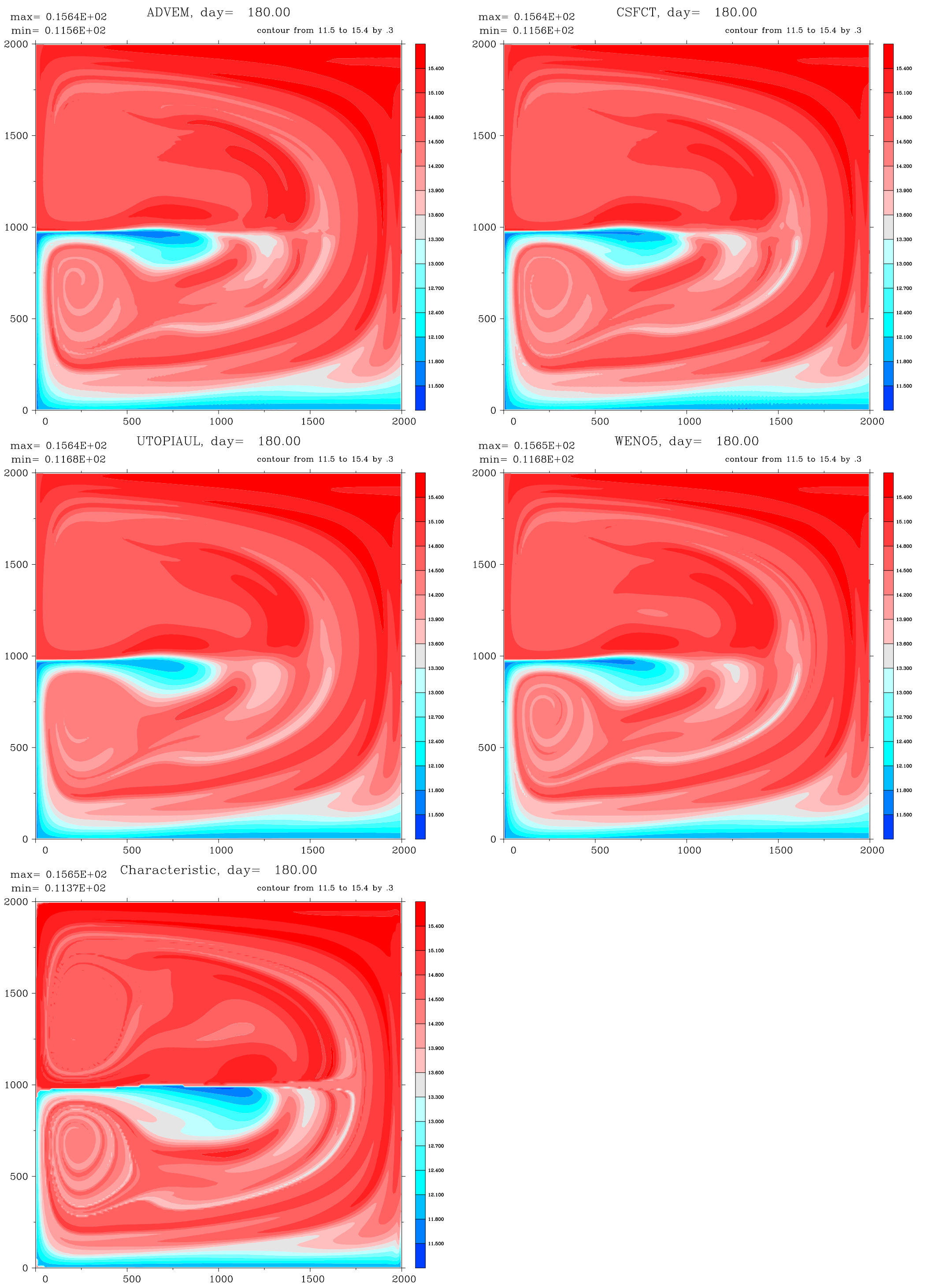

Figure 5: Same as figure 4 but for temperature.

in the jet region, and the salinity distribution in the recirculation zone. The Eulerian schemes have essentially dissipated to varying degree the sharp gradients created by the recirculating flow. Again, WENO5 exhibits the least dissipation in that region. CSFCT and ADVEM perform similarly while UTOPIA seems to smear gradients somewhat more then the others. The salinity minimum and maximum on either sides of the jet are eastward of the position calculated by the characteristic scheme. The temperature field is shown in figure 5 and exhibits the same characteristics. *Note: I thought I may be able to see differences between the numerical scheme to explain their behavior w.r.t. density, but there are no visual clues.*

Figure 6 shows contours of density anomaly at the end of 180 day simulations using the 4 different advection schemes. The largest positive density anomalies are primarily located along the jet axis where they are advected eastward. Their distributions seem to be independent of the advection scheme used. The density anomaly for WENO5 and UTOPIA is almost exclusively positive while those of CSFCT and ADVEM display positive and negative values. The negative anomalies are primarily located in the southwestern recirculation zone. These zone are particularly problematic since the tracers are continuously coiled into thinner and thinner filaments. Once the filaments' thickness becomes subgrid scale, it is smeared via either the TVD limiters or the inherent numerical dissipation of the scheme. The small scale noise in the CSFCT bears the fingerprints of the FCT limiters. The large gray areas are regions where the density anomaly magnitude is smaller then 10^{-3} sigma unit. The gray area expands as the advection scheme changes from ADVEM, to CSFCT, to UTOPIA and finally WENO5. Most of this expansion occurs in the south west side of the basin.

Figure 7 shows the evolution of various density anomaly norms with time. The plot of the density anomaly maximum and minimum confirm that the WENO5 and UTOPIA produce very small negative anomalies whereas ADVEM and CSFCT produce the largest such anomalies in magnitude. The minimum anomaly continues to decrease for ADVEM until day 400 before it starts to level off around -0.02 sigma units. The behavior of the positive density anomaly is similar in all schemes. After an initial growth period, of about 180 days, the maximum errors level off and remain pretty much constant. The density anomalies start appearing as progressive, originally smooth, tracers minima from the southern zone enter the jet and recirculation zones, and are juxtaposed next to tracer maxima from the northern gyre in ever thinning filaments. The 180 day period correspond to the time it takes for the temperature minimum located in the southwestern corner of the basin to reach the intense flow regions. ADVEM and CSFCT show very large episodic errors that peak around day 400 fopr ADVEM while the error variations are less pronounced for the other two schemes. WENO5 and UTOPIA perform best if judged based on the density anomaly extrema. The situation is less clear if one examins the root mean square error and the relative gain of mass in the entire basin. These errors are defined as:

$$\epsilon_1 = \frac{\sum_{i,j}(\sigma_\theta - \sigma_{\theta_0})}{MN\sigma_{\theta_0}} \qquad (20)$$

$$\epsilon_2 = \frac{\left[\sum_{i,j}(\sigma_\theta - \sigma_{\theta_0})^2\right]^{1/2}}{MN} \qquad (21)$$

and are shown in the lower left and upper right panels of figure 7. All schemes behave similarly in terms of these error norms, with a slight advantage to the CSFCT and

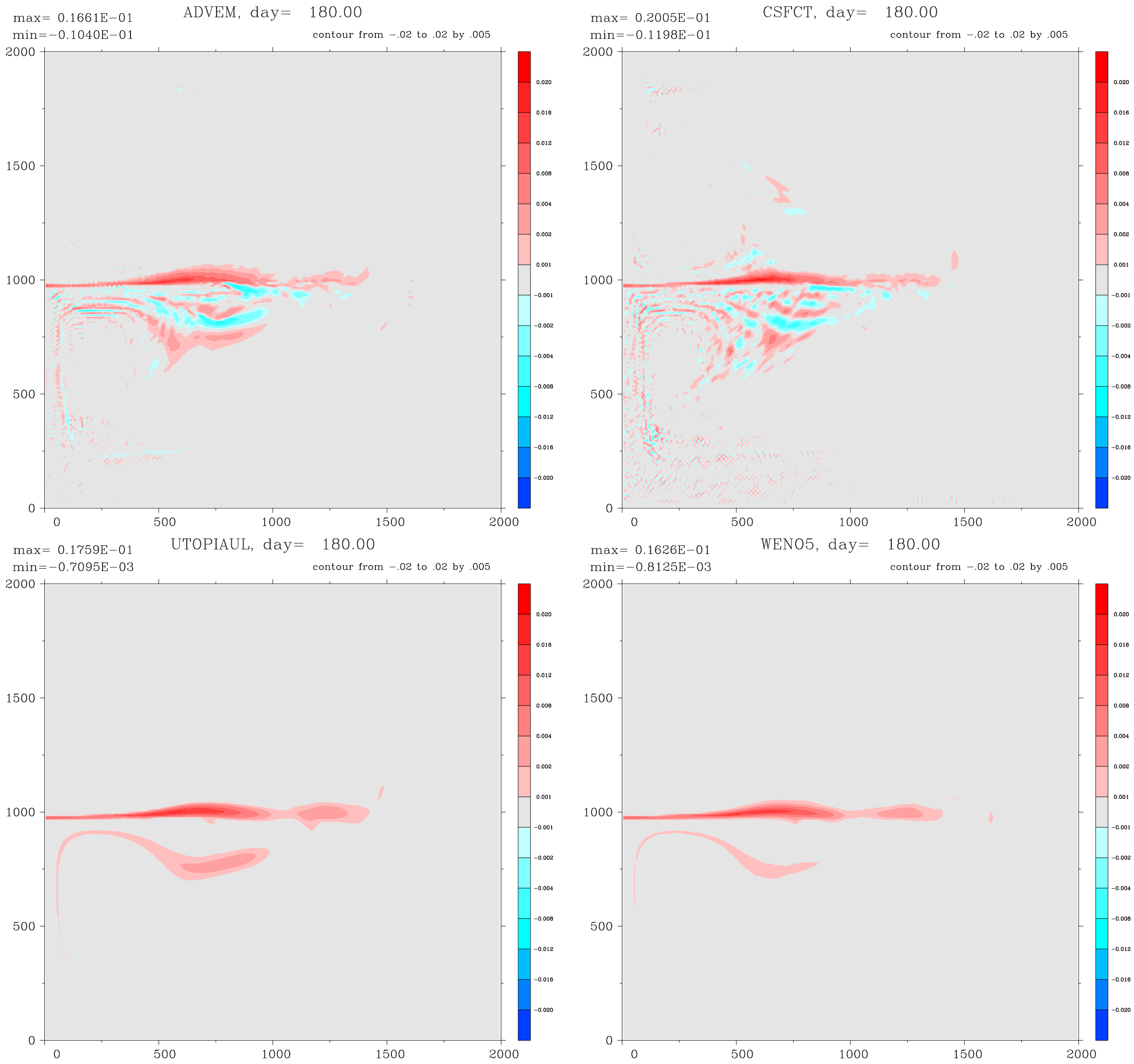

Figure 6: Errors in the density field after 6 months of simulation time. In row order we have ADVEM, CSFCT, UTOPIA-UL, and WENO5. Note that the contours levels are not linear but were chosen to highlight the density anomaly extrema. The regions where $|\Delta\sigma_\theta| < 10^{-3}$ are shown in grey.

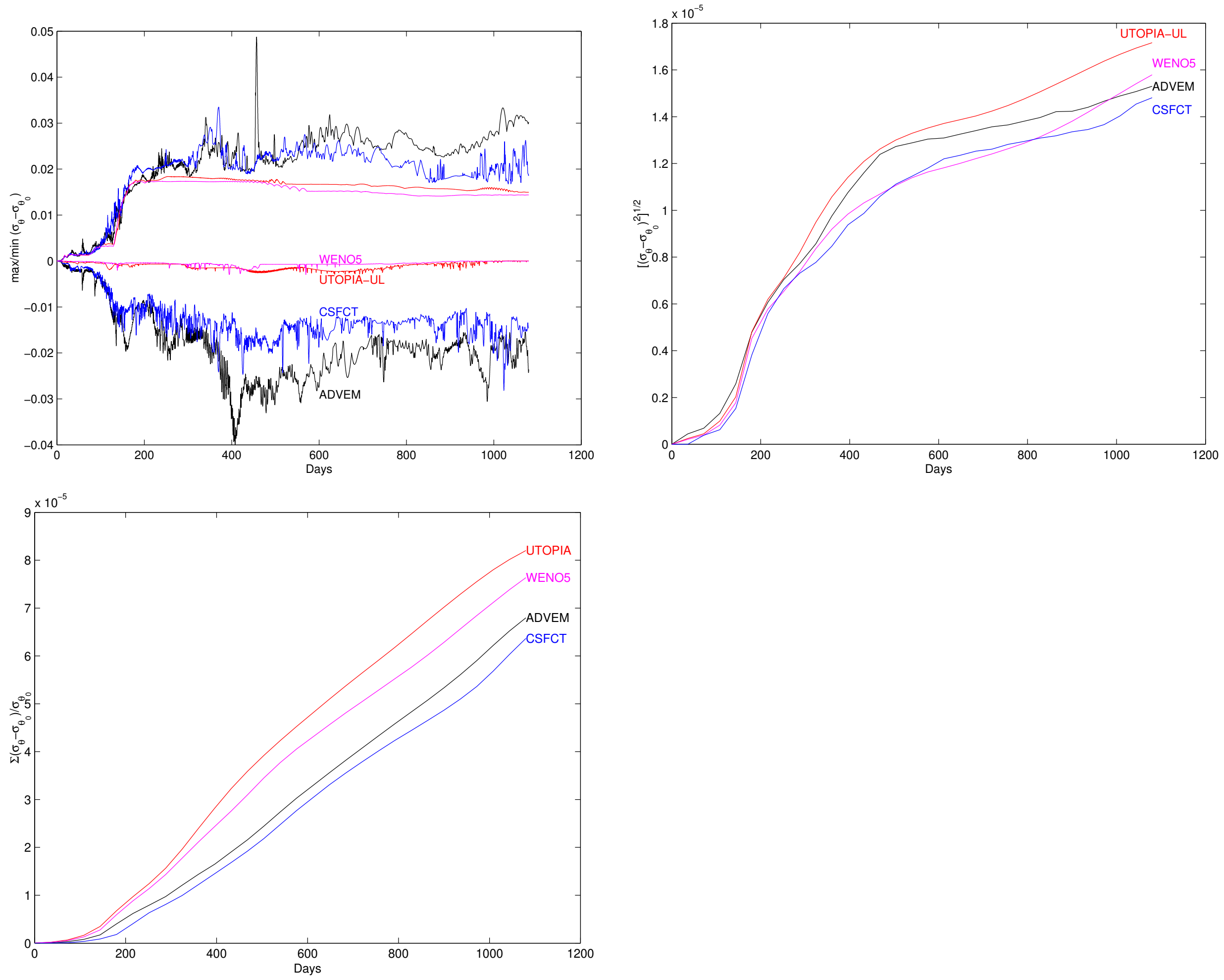

Figure 7: Density errors as a function of time for the 4 different numerical schemes. The top left figure shows the extrema (maximum and minimum density errors over the entire domain. The upper right figure shows the rms error, and the lower left figure shows the relative mass gain over the entire basin.

ADVEM scheme which lower global errors levels then WENO5 and UTOPIA; the differences are however small.

7 Heavier Density via changes in temperature

We repeat the previous experiment assuming the density corresponds to one of a deep layer (specifically layer 20 in Hycom with $\sigma_\theta = 27.82$). We accomplish this in two ways, via cooling or "salting".

In the first experiment, the water of layer 13 is artifically cooled to sink it to the depths of layer 20. Thus, the salt initial conditions are kept fixed and those of temperature are computed based on the nonlinear equation of state and the new density. The cooling reduced the minimum and maximum temperatures to 4.5 and 10.7 degrees, respectively, and thus has widened the temperature contrast. The temperature field at the end of a 180 day simulation is shown in figure 8 for the different schemes. Except for localized differences, the simulations look quite similar in their large scale features.

Figure 9 shows the density anomaly contours after 6 months of integration. The picture is largely the same as the previous one, figure 6. The main differences appear in the generation of even smaller scale errors in the southwestern recirculation zone for CSFCT and ADVEM. An elongated blob of higher anomalies also appear in that zone for WENO5 and UTOPIA but the smaller scale errors are absent. Figure 10 shows the temporal evolution of the different global density error norms. The increase in temperature contrast leads to a doubling of the density anomaly extrema. The negative anomalies are still small for UTOPIA and WENO5 although they do increase somewhat in magnitude. Likewise, there is a double of the error levels in the increased temperature experiment. One should note that the increased levels of density anomalies is not solely due to the increased contrast in density but also to increased curvature of the equation of state for those parameter regimes.

In the second experiment, the water of layer 13 is artifically salted to sink it to the depths of layer 20. This effectively increases the salinity maximum and minimum by about 1 unit each. The salinity field at the end of a 180 day simulation is shown in figure 11 for the different schemes. The picture is almost identical to the original experiment with density of 26.8. The density anomaly contours shown in figure 12 are almost identical to the one of figure 6 also. *Eric: we should probably remove the salting figures as they do not show much, except may for the integrated error measures.* Figure 13 shows the evolution of basin-wide density anomaly norms, they are about half as small as the ones of the previous experiment. We hypothesis that the equation of state is actually more linear for the present range of parameters.

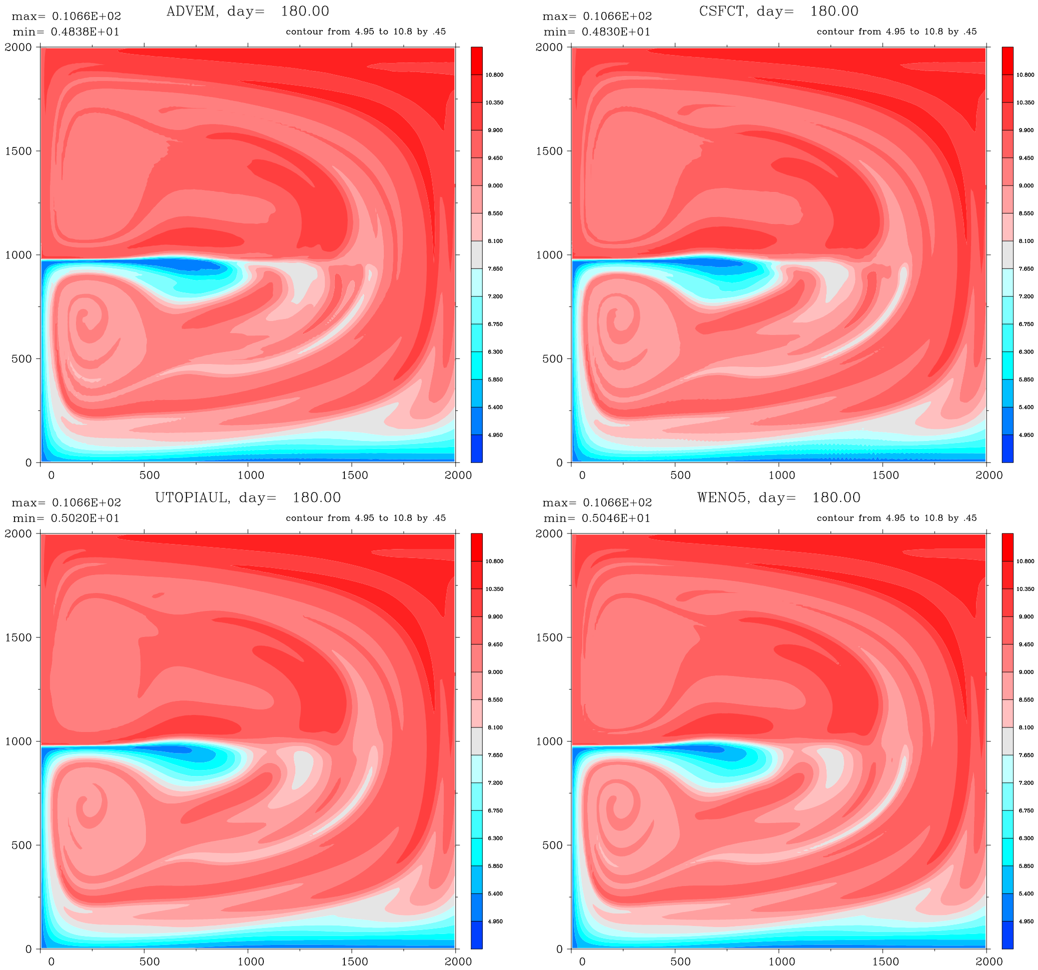

Figure 8: Same as figure 5 but for the equivalent deep layer temperature associated with $\sigma_\theta = 27.82$.

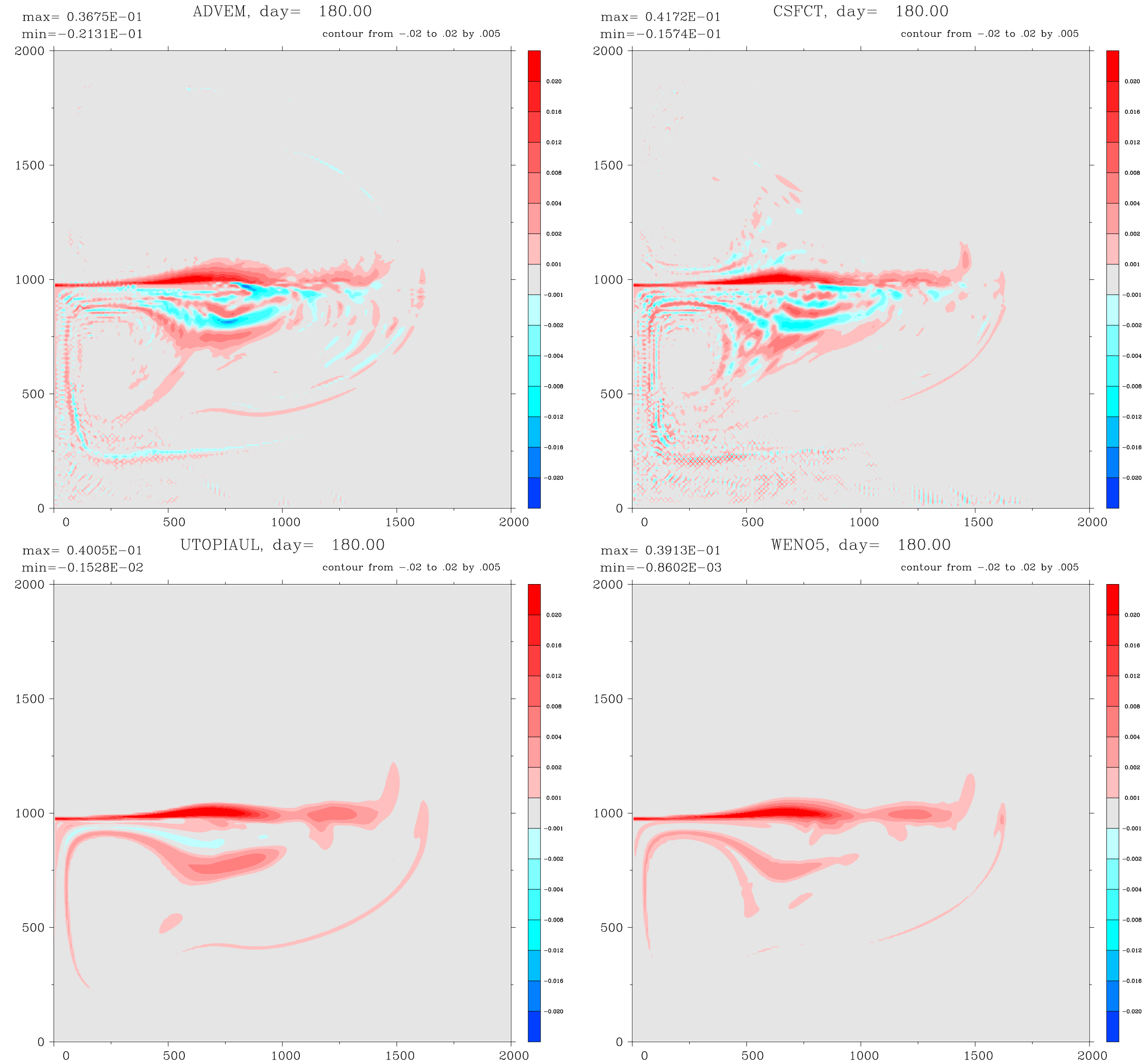

Figure 9: Density anomaly at day 180 for the cooling experiment. In row order we have ADVEM, CSFCT, UTOPIA-UL, and WENO5.

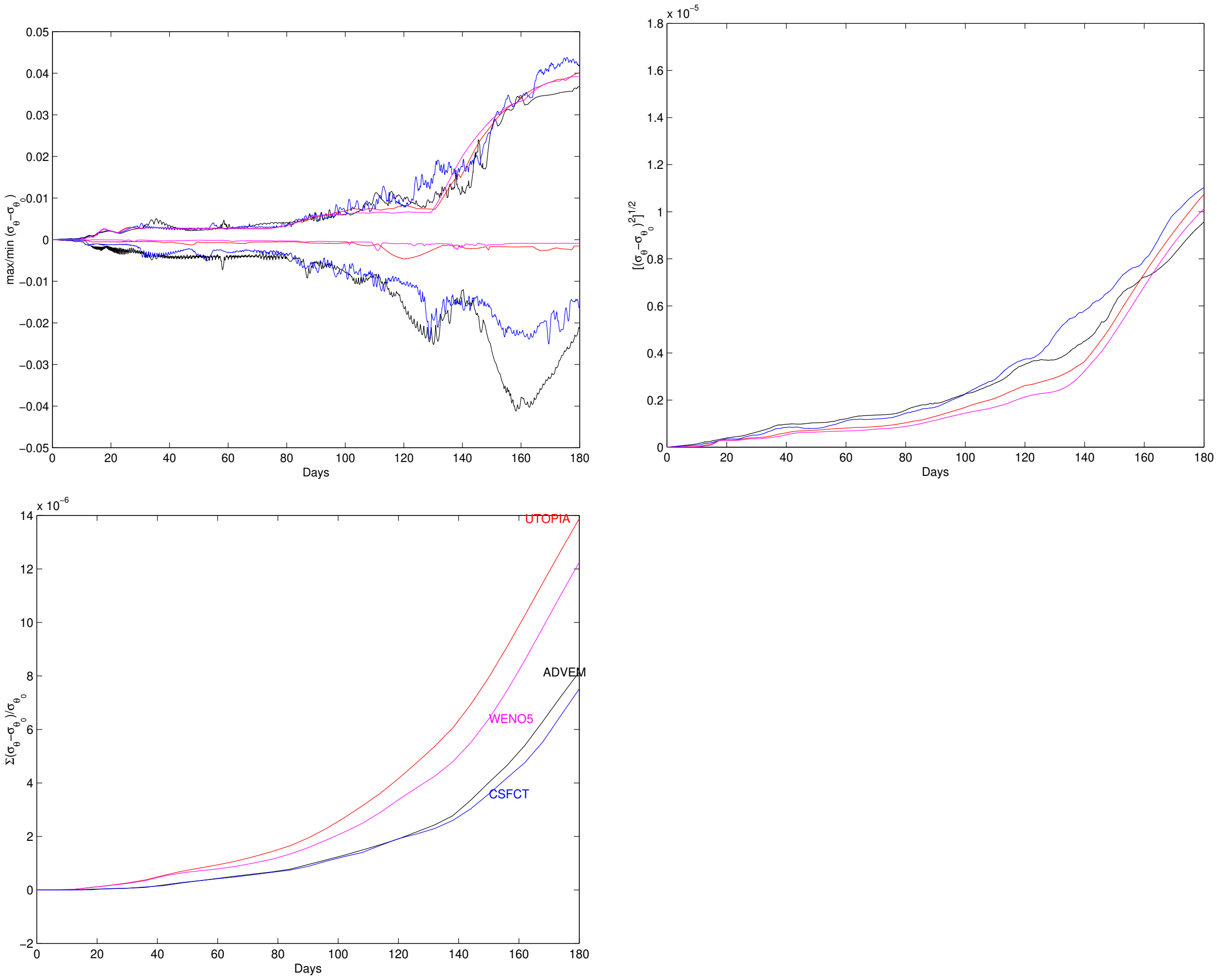

cc

Figure 10: Density errors as a function of time for the 4 different numerical schemes, and for the "cooling" experiment. The top left figure shows the extrema, the upper right figure shows the rms error, and the lower left figure shows the relative gain in mass.

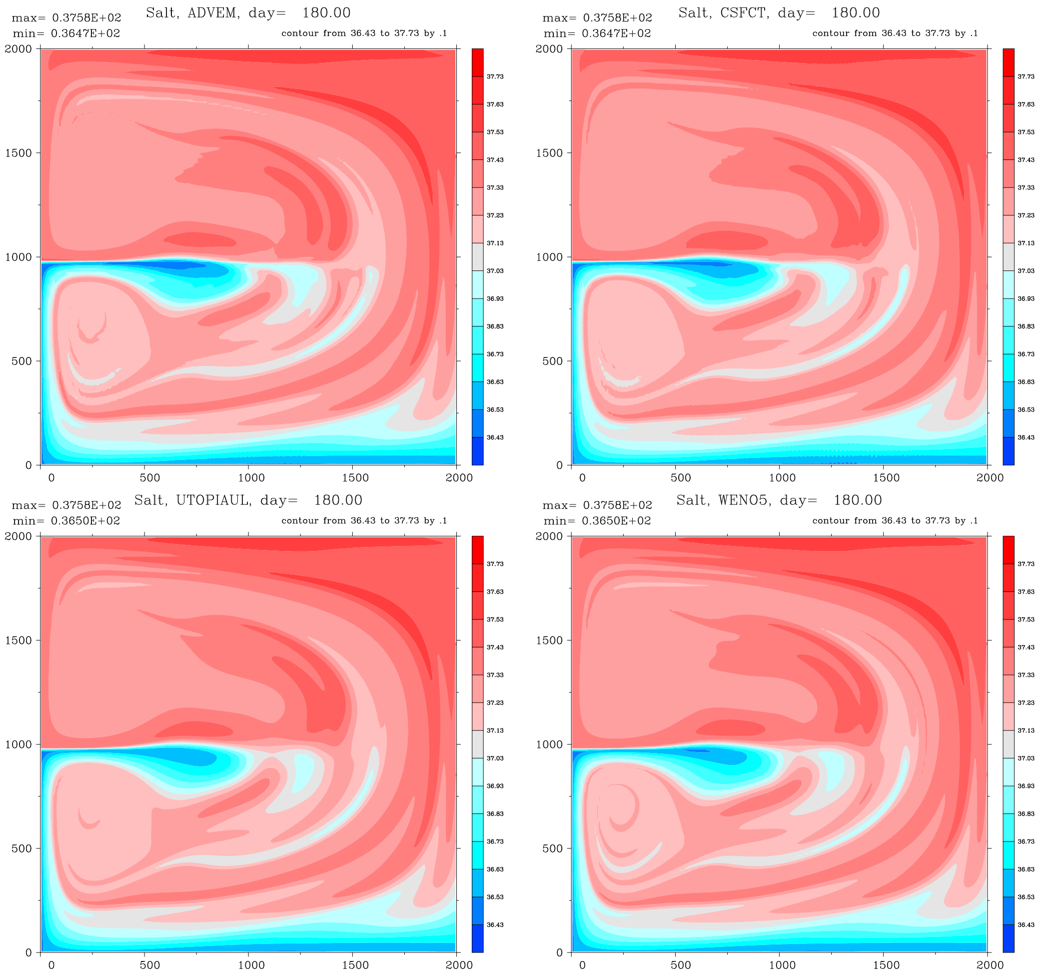

Figure 11: Same as figure 5 but for the equivalent deep layer salinity associated with $\sigma_\theta = 27.82$.

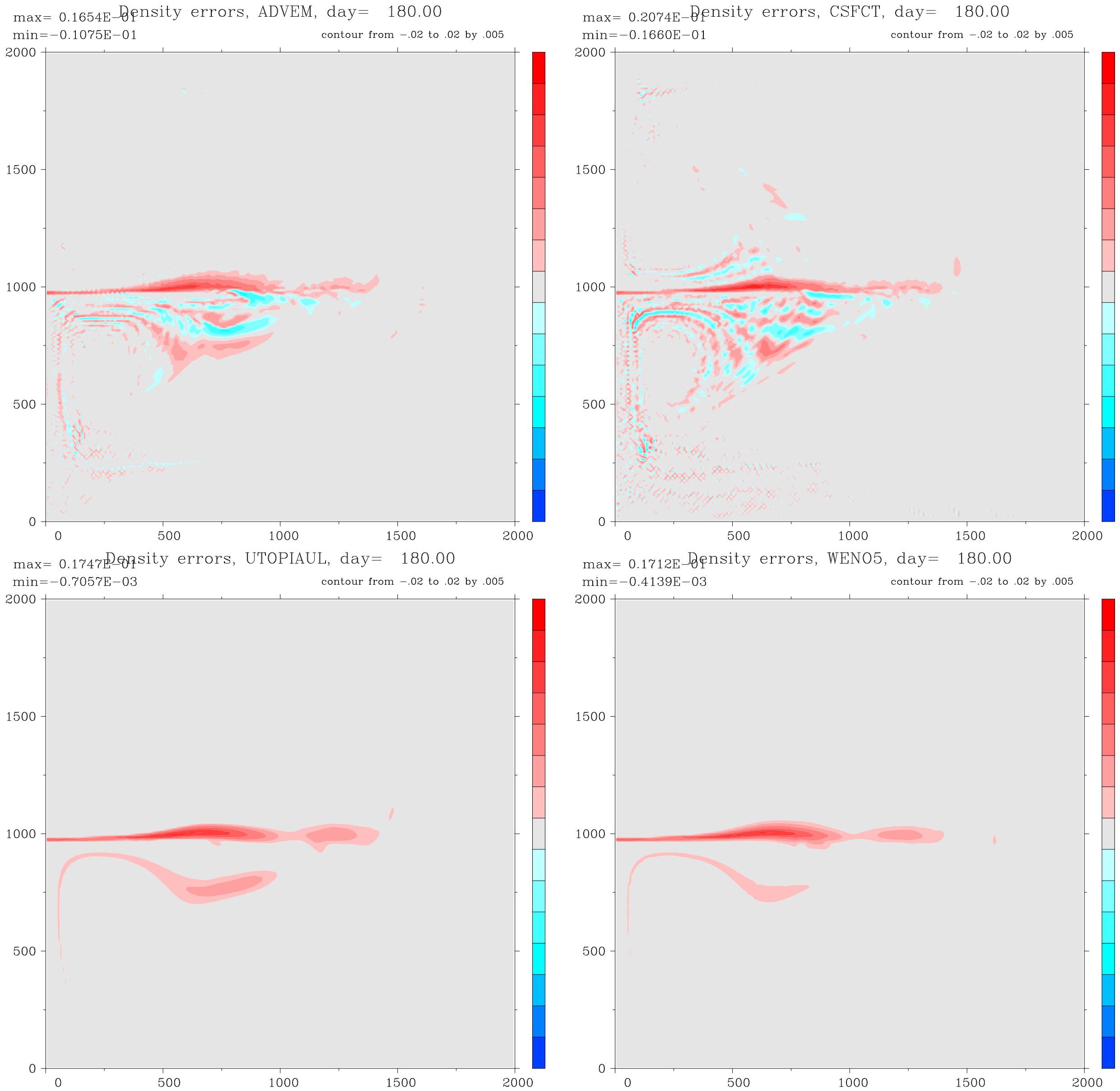

Figure 12: Density anomaly contours after 180 days of simulated time for the salting experiment. In row order we have ADVEM, CSFCT, UTOPIA-UL, and WENO5.

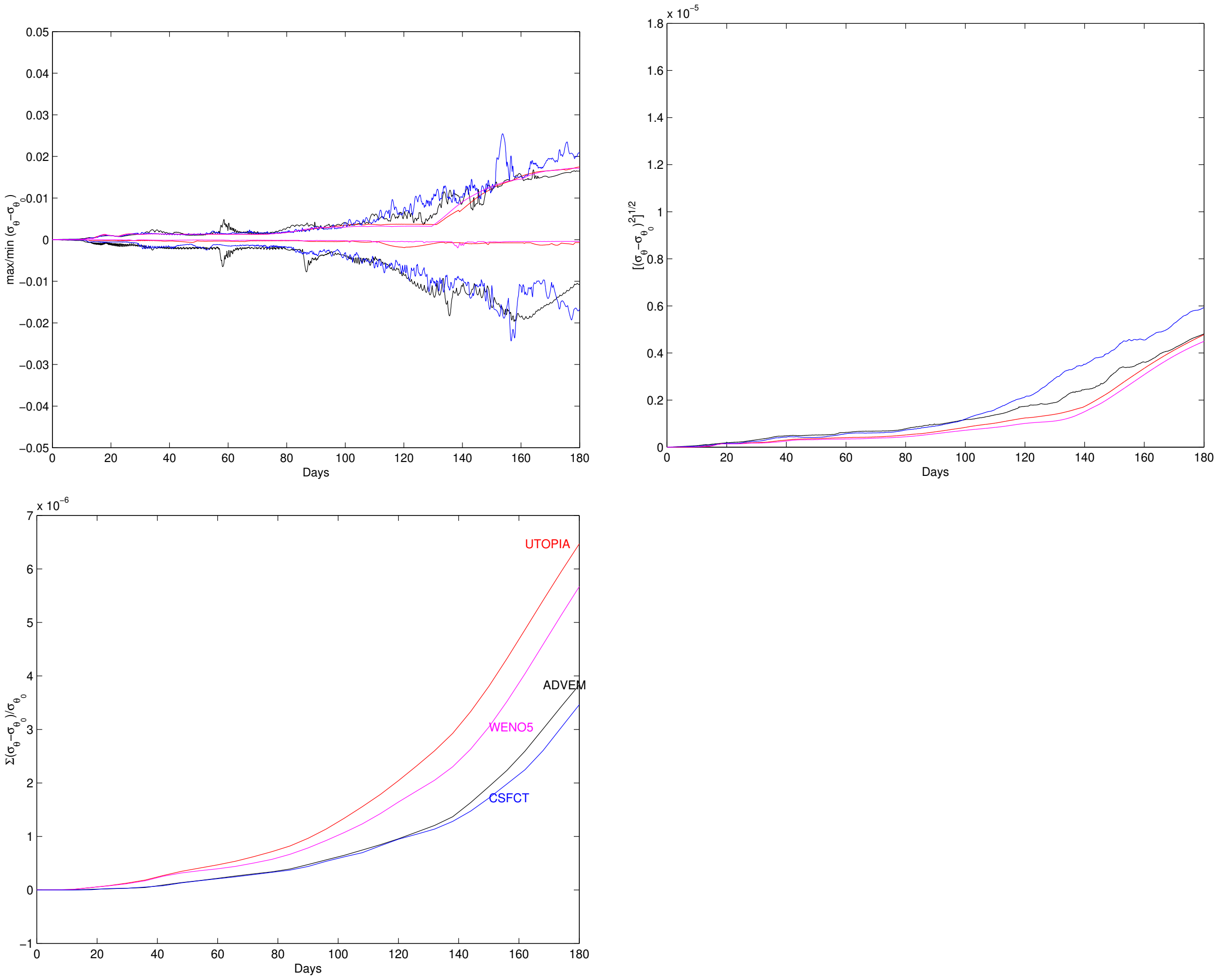

Figure 13: Density errors as a function of time for the 4 different numerical schemes for the "salting" experiment. The top left figure shows the extrema, the upper right figure shows the rms error, and the lower right figure shows the relative gain in mass.

8 Deep Layer Levitus T/S

We repeat our experiments using the Levitus T/S of layer 20 in HYCOM; the initial distribution are shown in figure 14. The north east features are reminiscent of Med outflow characteristic. A plot of the layer thickness (20-th layer in HYCOM) is shown in the lower left part of figure 14. The sizable layer thickness, in the range of 400-1100 meters, indicate that the aforementioned features, whatever their origins, are real. The only "masked-out" region occurs in the south western corner of the basin.

The simulation are carried out for a period of 3 years. The temportal evolution of the density error measures are shown in figure 15. The pattern is similar to the previous experiments, ADVEM and CSFCT exhibit short time episodes of large localized density anomalies, particularly negative ones; no such behavior is reported for UTOPIA or WENO5. Additionally, their negative anomalies are very small indeed while their maximum positive anomalies are 50% smaller then either CSFCT or ADVEM. The levels of positive density anomalies are similar for all schemes. The evolution of the root mean square error shows no significant difference between the schemes, and indicate, again, that the negative extrema must be quite localized in space. The error peaks occur around day 600 before levelling down. The error peaks are due to the initial conditions and for the time taken for the "prominent features" to recirculate in the western gyres.

The T/S field at the end of the integration are shown in figures 16 and 17, respectively. The "med outflow" features have dissipated after several recirculation cycles, and not much can be gleamed from the figures. The density errors at day 1080 are shown in figure 18. Unlike the previous cases, the largest errors are now found in the northern gyre while the southern gyre exhibit mostly low error levels. The explanation is probably related to the initial distribution of the T/S fields. In the previous experiments these features were located in the southern gyre and, hence recirculated in the southern gyre, while in the present experiment the most prominent features are located in the northern gyre. A plot of the density errors at day 600, figure 19, reveal the errors to originate from the jet zone before spreading primarily in the northern gyre.

9 Conclusion

We have investigated the impact of advection scheme on numerical cabbeling. We have shown that:

- Linear advection schemes will preserve linear correlations if the scheme is linear and constancy preserving. Experimentation with nonlinear schemes showed it to be true but we could not show it analytically. This is probably due to the fact that discontinuities are coincident in space for linearly coupled species and the limiters will be activated simultaneously for both tracers so that the coefficients are the same for the 2 tracers.
- Numerical cabbeling is a problem, particularly for the deep density layers where weak stratification dominate the dynamics.
- Even though the tracer distribution may initially be smooth, their advection through a deformational type of flow can lead to the generation of small scales

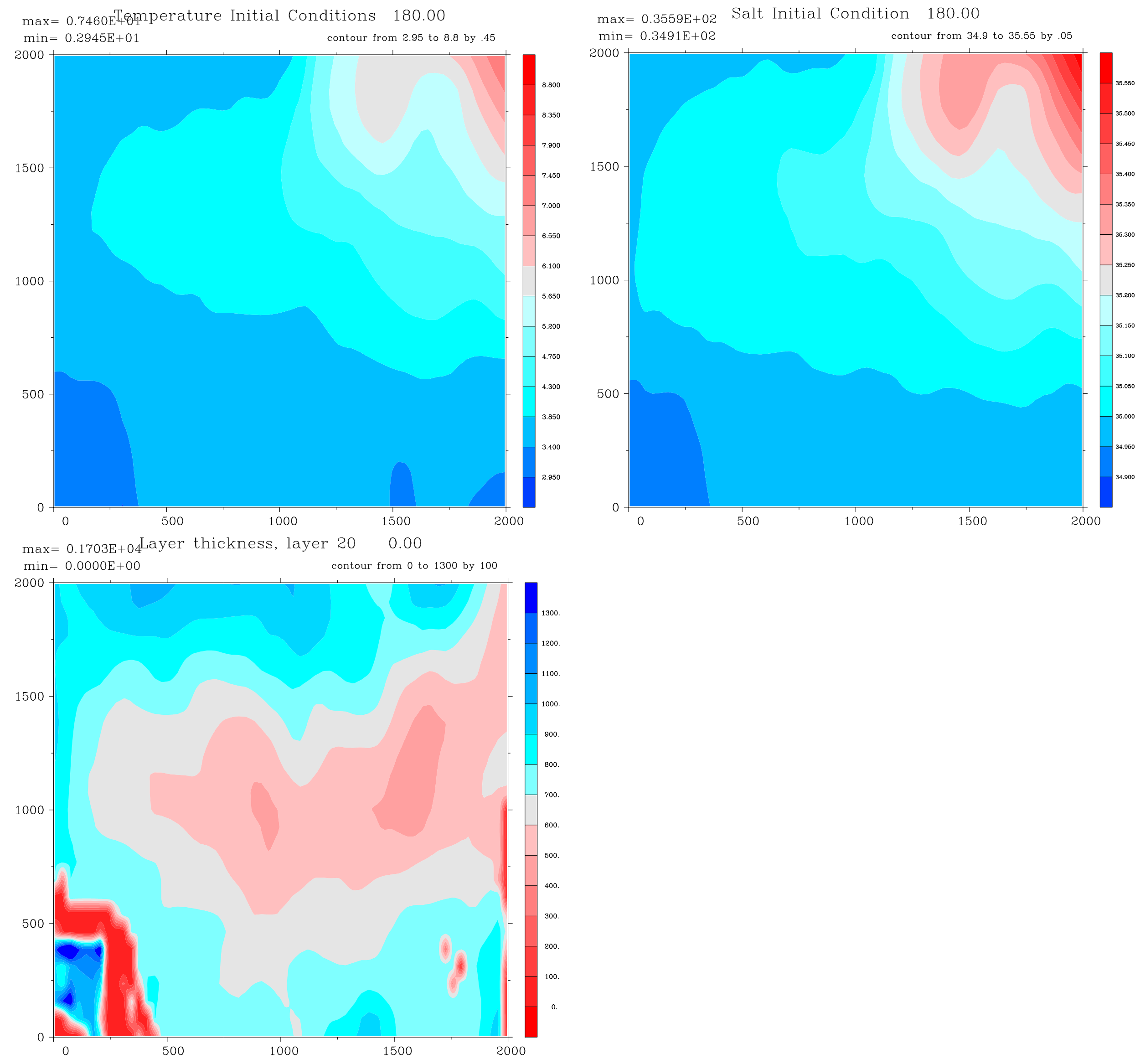

Figure 14: Initial conditions for the Levitus T/S fields whose combination yields a constant density of 27.82 sigma units. The lower layer shows the thickness of the 20-th layer in HYCOM

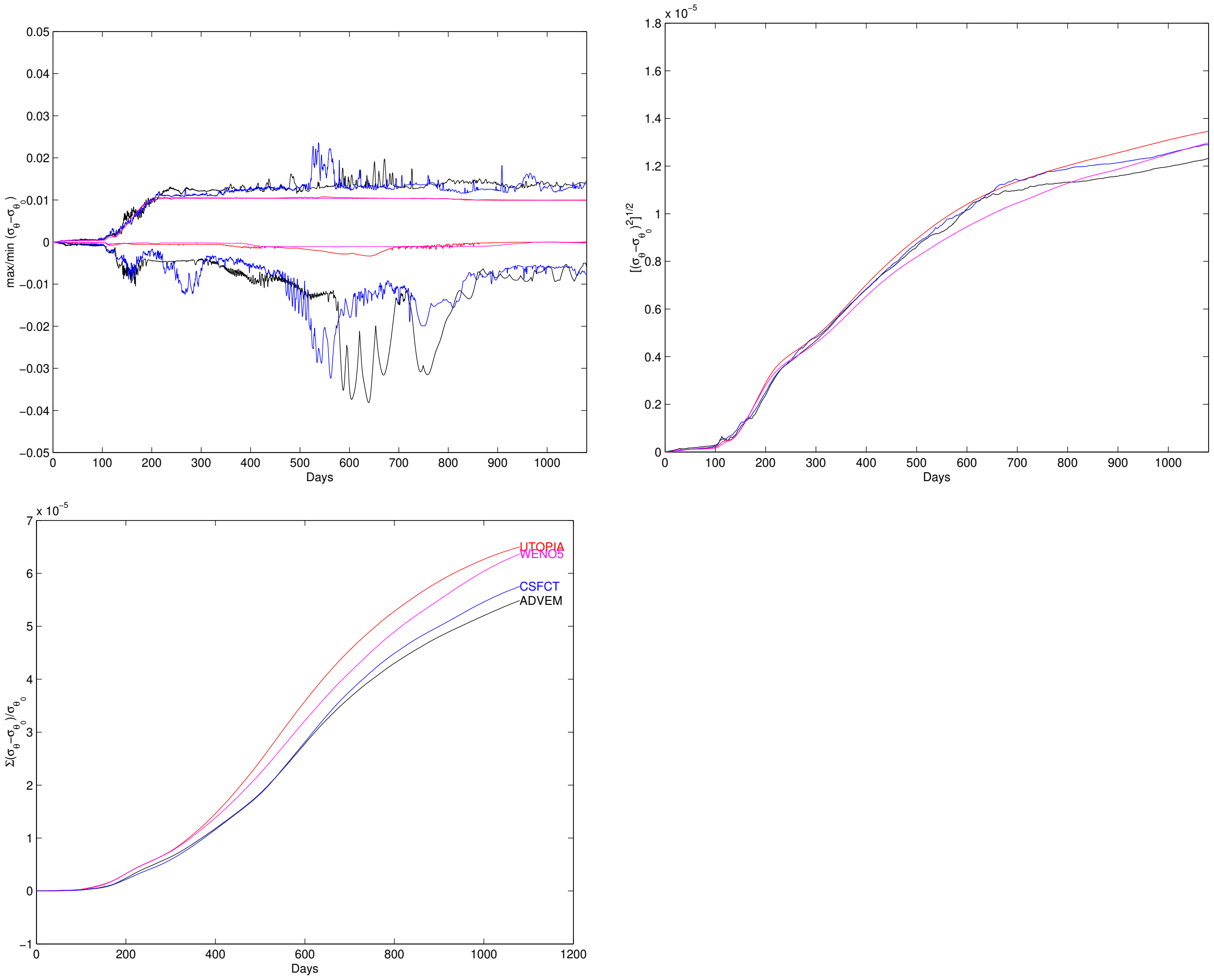

Figure 15: Density errors as a function of time for the 4 different numerical schemes, and for the deep Levitus T/S. The top left figure shows the extrema, the upper right figure shows the rms error, and the lower left shows the relative gain in mass

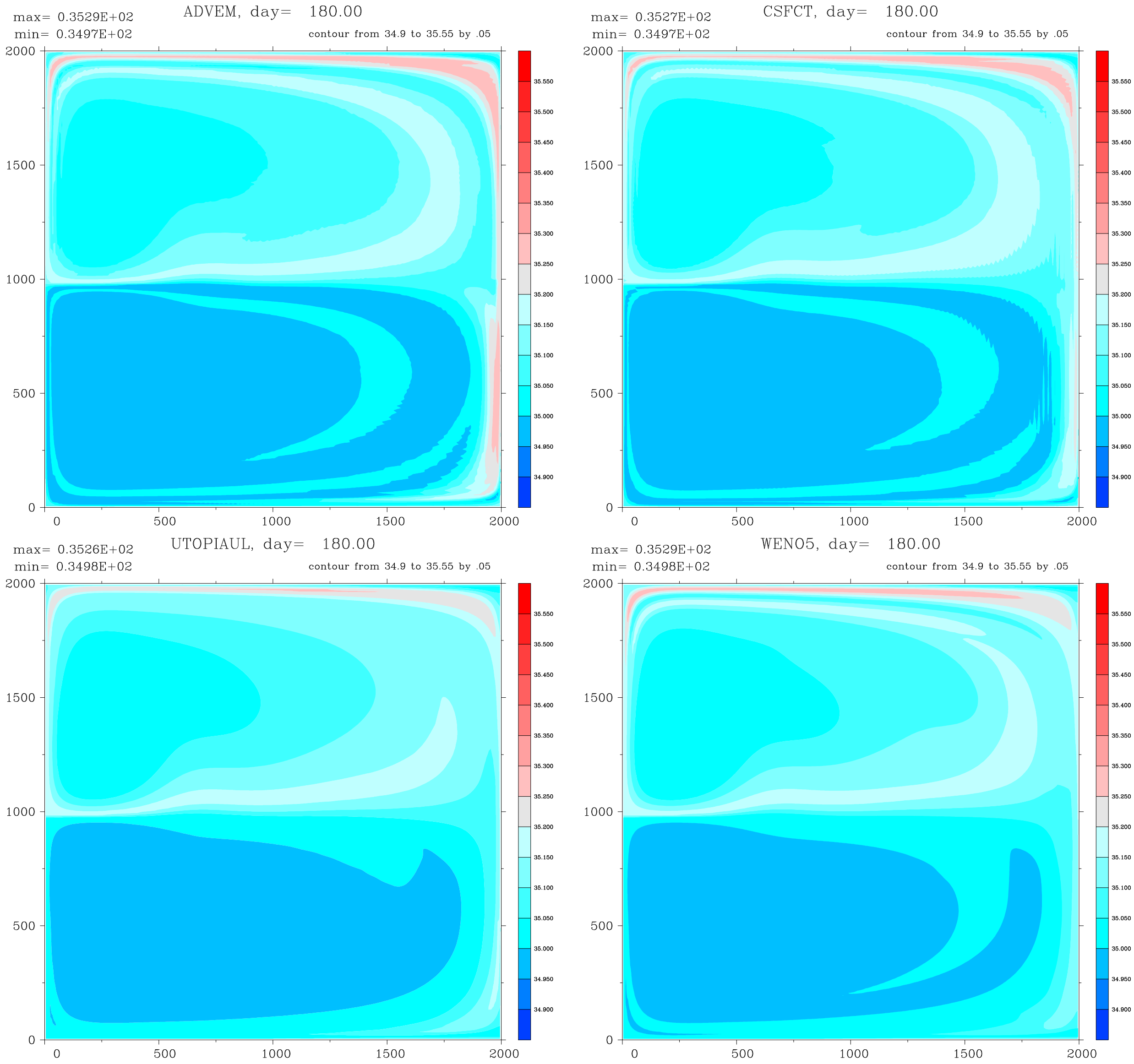

Figure 16: Deep layer salinity at the end of the simulation. In row order from top to bottom we have ADVEM, CSFCT, UTOPIA-UL, and WENO5. The color coding is the same as the other figures.

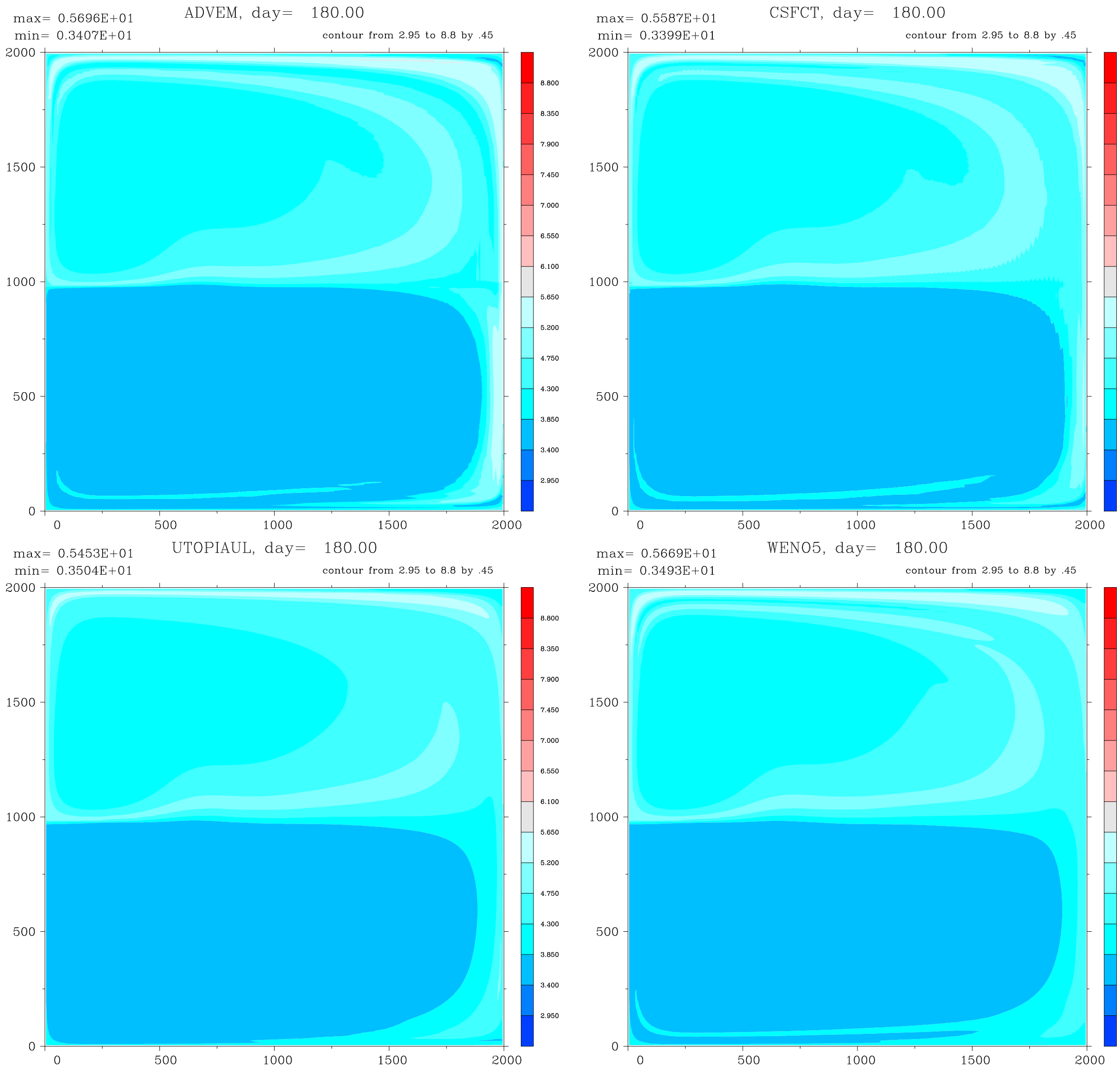

Figure 17: Same as figure 16 but for temperature.

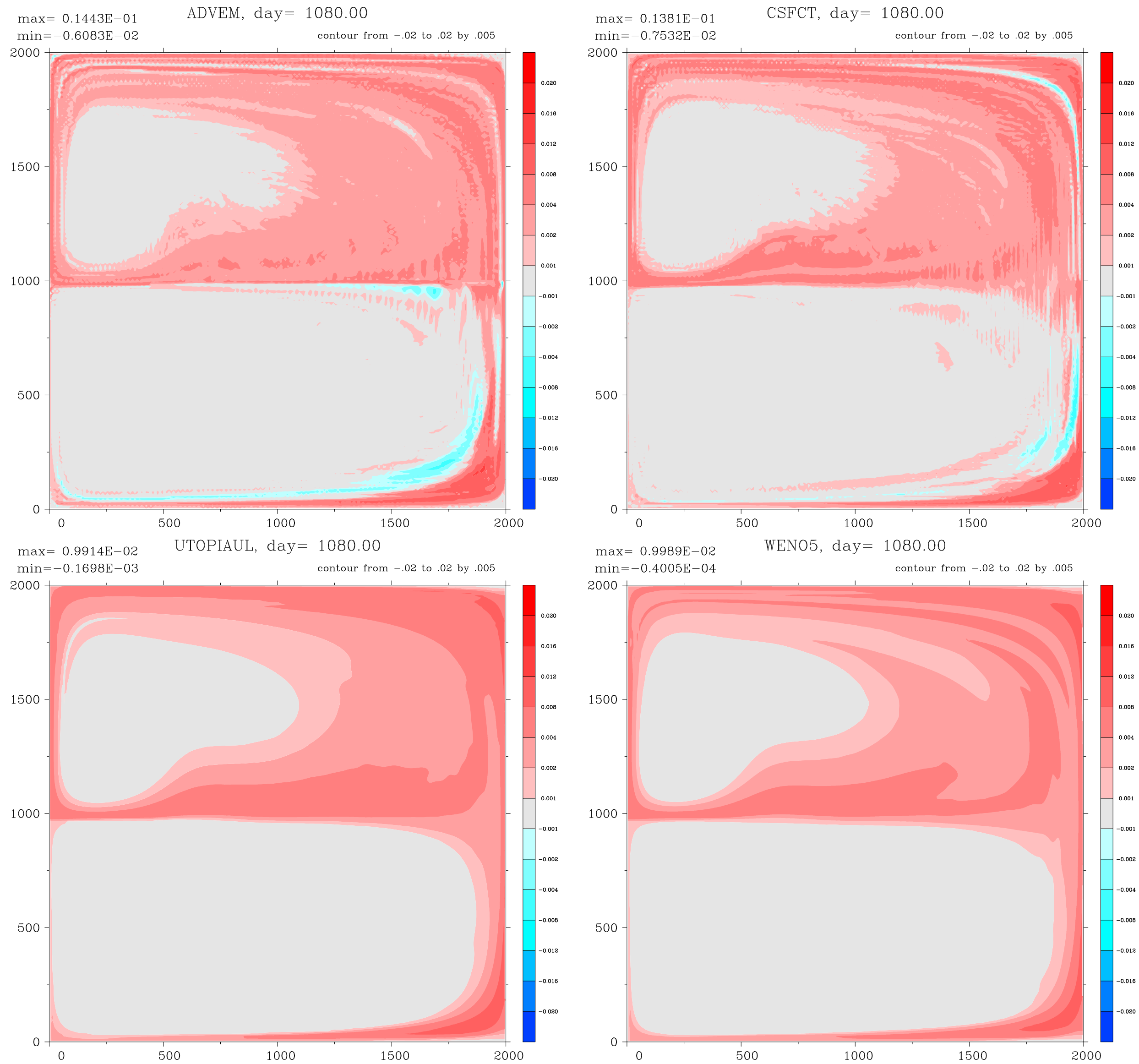

Figure 18: Errors in the deep layer density field at the end of the simulation, year 3. In row order we have ADVEM, CSFCT, UTOPIA-UL, and WENO5.

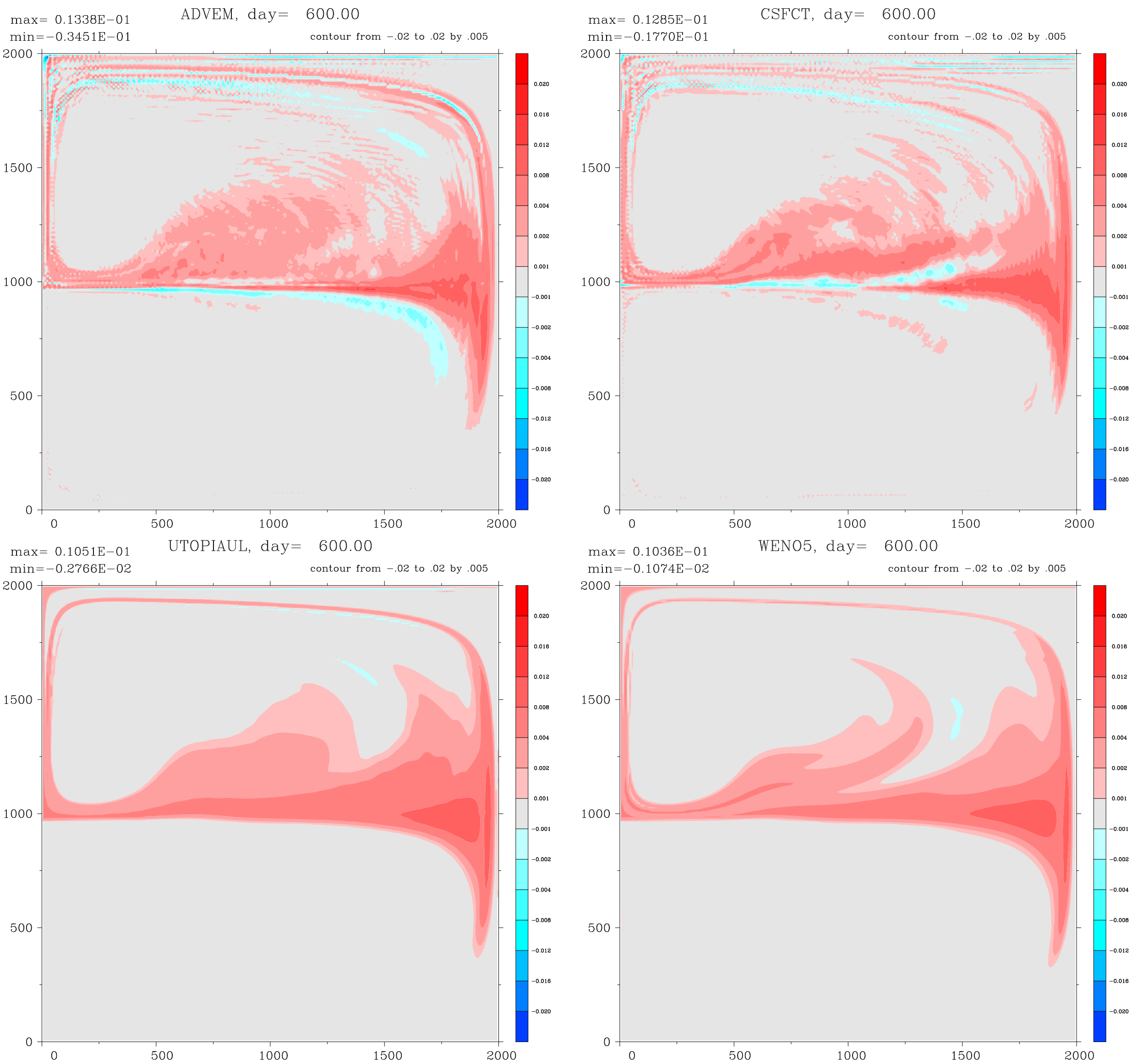

Figure 19: Errors in the deep layer density field at day 600 when negative errors peaked in ADVEM and CSFCT.

features. It is in the vicinity of these features that the numerical cabbeling is most intense.

- The centered type scheme a la ADVEM and CSFCT produce density anomalies of both signs (while cabbeling is understood to be production of denser water only). In contrast, the negative anomalies are almost absent from UTOPIA and WENO5. We speculate on the reasons. Both schemes are upstream biased and possess some form of hyperviscous operator; the latter removes the unresolved scales from the solution continuously. The FCT limiters on the other hand are notorious for producing terracing effect and may lead to the occasional generation of small scale features whose removal is less systematic.
- As a consequence of the above, WENO5 and UTOPIA tend to accumulate more mass in the basin then the other two techniques.
- We have not touched on the subject of mitigating the numerical cabbeling. This will be left to another paper.

This research was supported with grants from ONR under contract blablabla. We would like to thank Linda Smith for providing the T/S Levitus data used in layer 13 and 20 of HYCOM, plus other people.

A Density Equations

The equations governing the evolution of density in a nonhomogeneous fluid are not trivial if one considers their derivation from basic physical principals. Standard texts usually consider the case of a homogenous fluid where the contribution of salinity to the equation of state is missing; when salinity is included, it is usually via a linear equation of state. The inclusion of salinity effect is complicated by the repeated reference to thermodynamic relations when deriving the temperature equation from the internal energy equation. This section retraces the steps taken when deriving the temperature and salt equations.

The principle physical laws governing the evolution of density for a homogeneous fluid are: [2, 6] mass conservation, energy conservation, and the equation of state. In mathematical terms these are given by:

$$\frac{\mathrm{d}\rho}{\mathrm{d}t} + \rho \nabla \cdot \mathbf{u} = 0 \tag{22}$$

$$\frac{\mathrm{d}T}{\mathrm{d}t} - \frac{\alpha T}{C_p \rho}\frac{\mathrm{d}p}{\mathrm{d}t} = \kappa_T \nabla^2 T + \frac{\Phi}{C_p} + \frac{Q}{C_p} \tag{23}$$

$$\rho = \rho(p, T, S) \tag{24}$$

23 represent the The three terms on the right hand side of equation23 stand for heat diffusion, heat addition due to viscous dissipation, and heat sources. The second term on the right hand side of the equation represents the work done on the fluid. The different coefficient appearing in the equations are: the coefficient of thermal expansion $\alpha = \frac{-1}{\rho} \left.\frac{\partial \rho}{\partial T}\right|_p$, the specific heat at constant pressure $C_p = T \left.\frac{\partial s}{\partial T}\right|_p$, the heat diffusion coefficient κ_T.

The conditions that a fluid be incompressible are:

1. The fluid velocity is much smaller then sound waves: $U/c \ll 1$ where $c = \frac{\partial \rho}{\partial p}$ is the sound wave speed.
2. the wave phase speed is much smaller then sounds waves $C/c \ll 1$
3. the density scale height is smaller then the depth of the fluid
4. density changes due viscous forces, and molecular diffusion of heat and salt are small.

Since these conditions are well realized in the ocean, we take the fluid to be incompressible. The mass conservation equation becomes a constraint on the fluid velocity to be solenoidal, and the density ceases to play a role in mass conservation. We are thus left with the energy equation and the equation of state.

The energy conservation equation can be simplified by first invoking the incompressibility condition, and dispensing with heat generation due to viscous action. In the absence of heat sources, energy conservation reduces to a temperature evolution equation of the form:

$$\frac{\mathrm{d}T}{\mathrm{d}t} = \kappa_T \nabla^2 T \tag{25}$$

For water in the ocean the equation of state depends on pressure, temperature and salinity. The governing equations must thus be supplemented with a salt conservation equation to close the system:

$$\frac{\mathrm{d}S}{\mathrm{d}t} = \kappa_S \nabla^2 S \tag{26}$$

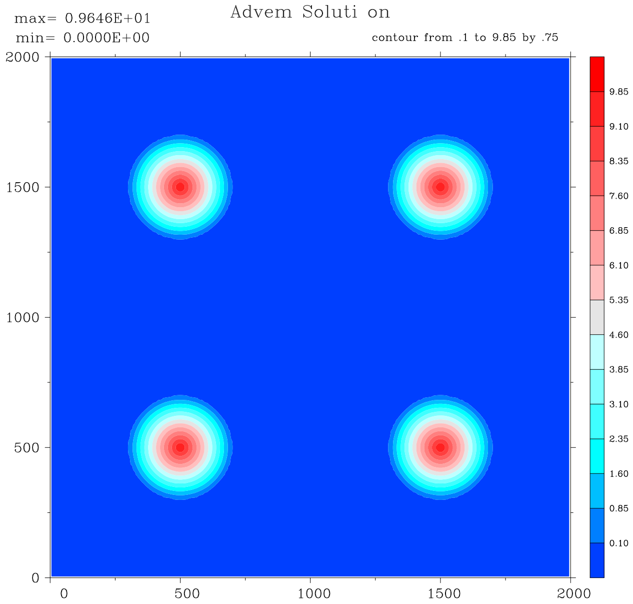

Figure 20: Initial tracer distribution for the shallow water tests

where κ_S is the coefficient of salt diffusion.

B Characterization of the numerical schemes

This section is devoted to the validation and characterization of the different advection schemes when the flow field obeys the continuity equation 17. The setting is similar to the rotating cone experiment where the initial tracer distribution is given by:

$$\begin{aligned} T(x,y,0) = 2 \quad &+ \quad \max\left(0, 1-\frac{r_1}{200}\right) + \max\left(0, 1-\frac{r_2}{200}\right) \\ &+ \quad \max\left(0, 1-\frac{r_3}{200}\right) + \max\left(0, 1-\frac{r_4}{200}\right) \end{aligned} \tag{27}$$

where r_i is the distance in km to the four points $(x, y) = (1000 \pm 500, 1000 \pm 500)$. A contour plot of the initial distribution is shown in figure 20 and shows four blobs at varying distance from the western boundary current, recirculation and jet regions. The advection equation is integrated for 222 days using a 40 minute time step. In order to compare the different solutions obtained, we will compute a reference solution using the method of characteristic. The time integration for the trajectory used a Runge Kutta method with adaptive step size control and a Richardson (rational) extrapolation (deffered approach to the limit of $\Delta t = 0$) to calculate the foot of the characteristic. This reference solution is shown in the lower right panel of figure 21. The western blobs are entrained into the WBC system with some portions recirculating several times during the course of the simulation; this recirculation creates zones of alternating low and high tracer values. The eastern blobs are slowly entrained into the western boundary current.

Figure 21 compares the different numerical solutions obtained with WENO, UTOPIA-UL, and the standard tracer advection scheme in HYCOM. The three schemes yield

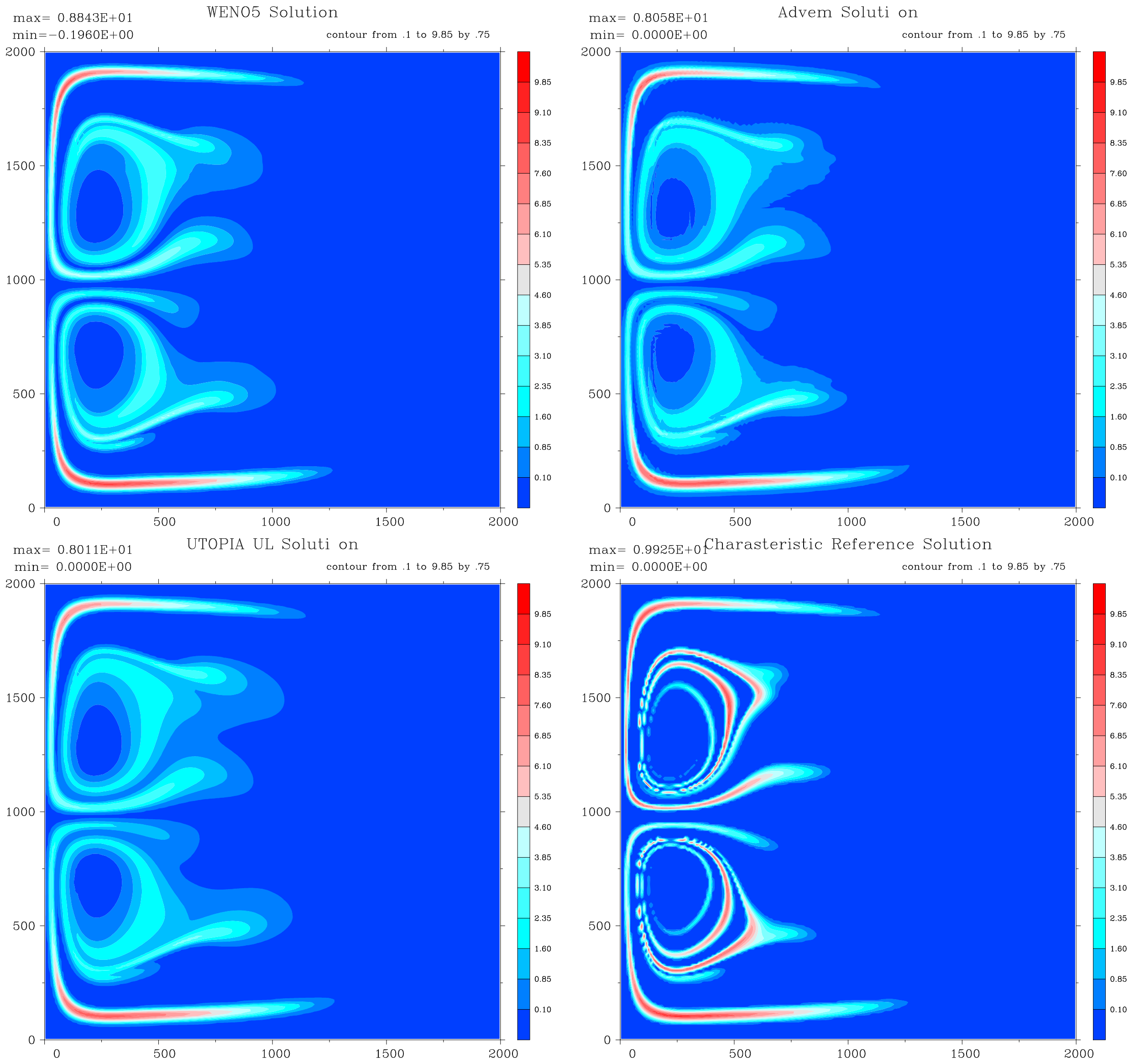

Figure 21: Comparison of different numerical scheme for the solution of the advection equation. The reference solution was obtained with a characteristic method. The contours were drawn after substracting 2 from the solution.

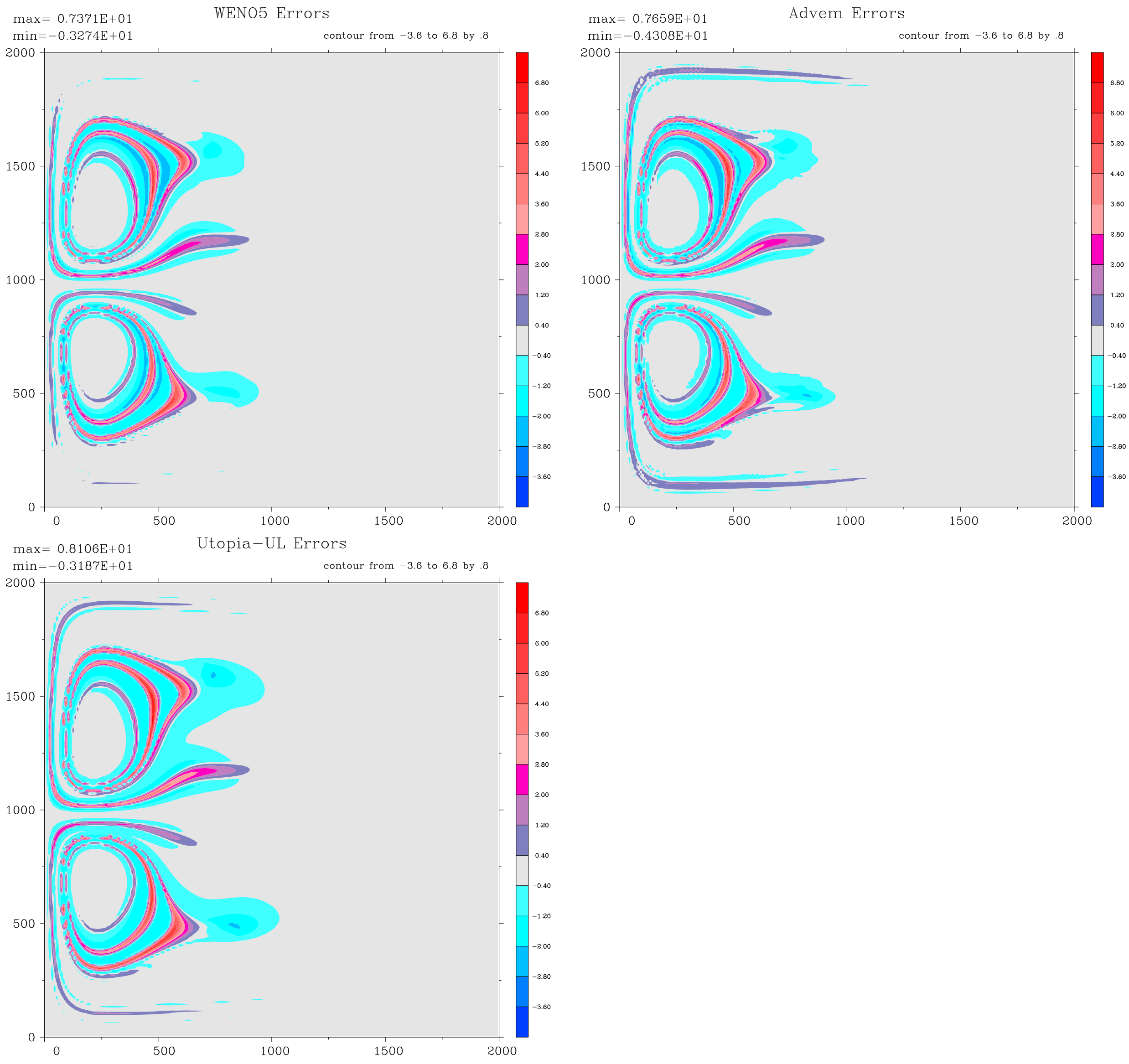

Figure 22: Contour plot of the numerical solution minus the reference solution. The 2 lower panels show the impact of the mean value of the field on the advem solution.

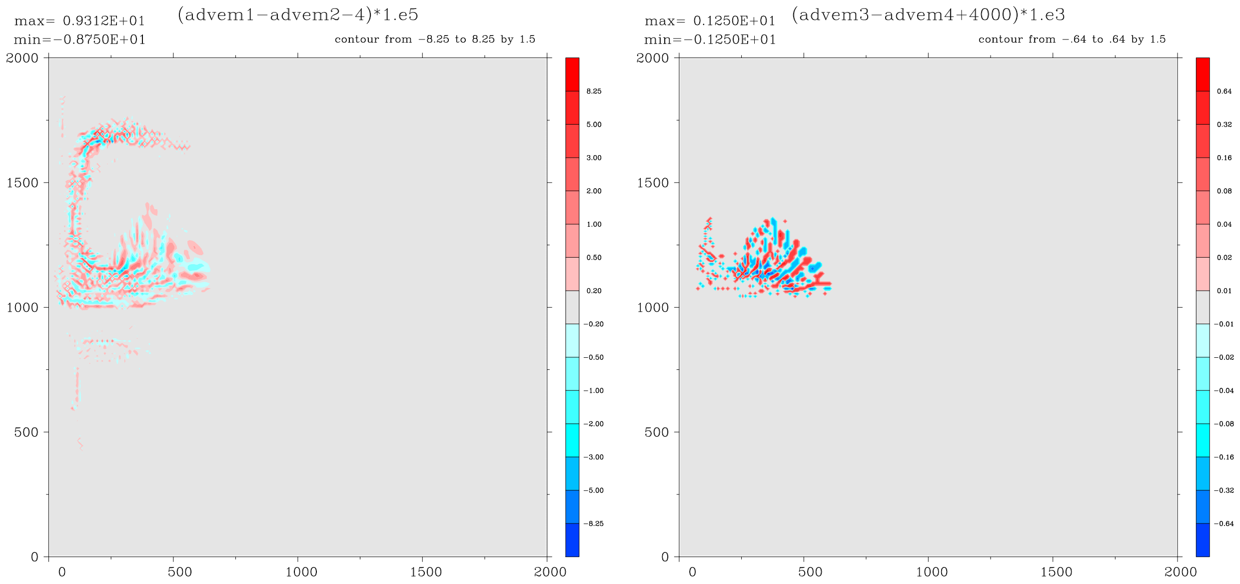

Figure 23: Impact of the mean value of the field on the advem solution.

similar solutions at a qualitative levels. The tracers flowing through the western boundary current system is subject to a substantial amount of numerical dissipation; the pattern is of course more pronounced for those portions caught in the recirculation zones. There is also substantial smearing of the frontal regions as the western blobs are coiled through the recirculation zone. The loss of peak is most severe for UTOPIA and advem and is approximated 20%, as opposed to 12% for WENO5. It is important to note that only WENO5 does not rely on limiters. There are some oscillations in the advem solution, probably some terracing effect due to the limiter. These effects are probably absent from the UTOPIA solution because of its inherent (hyperviscous) dissipation. The plot of the difference between the numerical and reference solution is shown in figure 22 and confirm the similar performance of the different schemes. The major difference between the different schemes are the elevated errors levels in advem in the northern and southern boundaries (the paths of the eastern blobs), were lower values of tracers are recorded compared to the reference solution. The level of numerical dissipation is however the same in the western boundary current region.

MPDATA is known to be sensitive to the mean value of the advected field (the addition of a constant value leads to a difference in the solution). We confirmed this sensitivity for the case of a divergent flow field. The initial condition in this experiment is obtained by substracting four uniformly from the initical conditions of the previous experiment. The difference between the two advem solutions is shown in the lower right panel of figure 23. The error in this example are indeed small (but finite), the errors were multiplied by 10^5 to make the labels on the colormap visible. Most interestingly, the errors are not symmetrically distributed between the 2 gyres, but are primarily located in the northern gyre. The difference must be due to the change in layer thicknesses as the blobs move westward: The northern blobs undergo compression whereas the southern blobs feel the expansion of the layer thickness. A similar conclusion can be drawn for the lower right panel of figure 23 where the background constant in the initial value of the field has been changed to ± 2000. The difference between the 2 solutions appear primarily in the northern gyre; their amplitude is two order of magnitude greater then the one in the left hand panel.

References

[1] D.S. Balsara and C.-W. Shu. Monotonicity preserving weighed essentially non-oscillatory schemes with increasingly high order of accuracy. *Journal of Computational Physics*, 405–452:160, 2000.

[2] G. K. Batchelor. *Introduction to Fluid Dynamics.* Cambridge University Press, Cambridge, 1967.

[3] D. R. Durran. *Numerical Methods for Wave Equations in Geophysical Fluid Dynamics.* Springer, New York, 1999.

[4] S. Gottlieb and C.-W. Shu. Total variation diminishing runge-kutta schemes. *Mathematics of Computations*, 67(221):73–85, 1998.

[5] B.P. Leonard, M.K. MacVean, and A.P. Lock. The flux integral method fo multidimensional convection and diffusion. *Applied Mathematical Modelling*, 19:333–342, 1995.

[6] J. Pedlosky. *Geophysical Fluid Dynamics.* Springer-Verlag, New York, 1987.

[7] P. Rasch. Conservative shape preserving two dimensional transport on a spherical reduced grid. *Monthly Weather Review*, 122u:1337–1350, 1994.

[8] R. Sadourny. The dynamics of finite-difference models of the shallow water equations. *Journal of Atmospheric Sciences*, 32:680–689, 1975.

[9] C.-W. Shu. *Essentially non-oscillatory and weighed essentially non-oscillatory schemes for hyperbolic conservation laws*, page 325. Springer, New York, 1998.

[10] P.K. Smolarkiewicz and L.J. Margolin. Mpdata: A finite difference solver for geophysical flows. *Journal of Computational Physics*, 459–480:140, 1998.

[11] A. Staniforth, J. Cote, and J. Pudykiewicz. Comments on smolarkiewicz's deformational flow. *Monthly Weather Review*, 115:894–900, 1987.

[12] A. Suresh and H.T. Huynh. Accurate monotonicity preserving schemes with runge-kutta time stepping. *Journal of Computational Physics*, 136:83–99, 1997.

[13] J. Thuburn. Multidimensional flux-limited advection schemes. *Journal of Computational Physics*, 123:74–83, 1996.

[14] S.T. Zalesak. Fully multidimensional flux-corrected transport algorithms for fluids. *Journal of Computational Physics*, 31:335–362, 1979.